Multi-objective Design and Performance Analysis of Incremental Control Allocation-based Flight Control Laws

Pollack, T.S.C.; van Kampen, E.

DOI
10.2514/6.2023-1249

Publication date
2023

Document Version
Final published version

Published in
AIAA SciTech Forum 2023

Citation (APA)
Pollack, T. S. C., & van Kampen, E. (2023). Multi-objective Design and Performance Analysis of Incremental Control Allocation-based Flight Control Laws. In *AIAA SciTech Forum 2023* Article AIAA 2023-1249 (AIAA SciTech Forum and Exposition, 2023). https://doi.org/10.2514/6.2023-1249

AIAA SciTech Forum
23-27 January 2023, National Harbor, MD & Online
AIAA SCITECH 2023 Forum

10.2514/6.2023-1249

Multi-objective Design and Performance Analysis of Incremental Control Allocation-based Flight Control Laws

T.S.C. Pollack*, and E. van Kampen†
Delft University of Technology, 2629HS Delft, The Netherlands

The functional architecture of a flight control system (FCS) is driven by multiple objectives related to the aircraft's operational mission and in-service performance targets. Control allocation (CA) is a common method to ensure adequate use of the available effector architecture once the number of control effectors linked to the FCS increases and the control problem becomes overdetermined. A primary CA design objective is to ensure that high-level motion control demands are met. However, the additional degrees of freedom offered by the control effector suite can also be exploited to perform secondary control tasks. In this light, this article focuses on the Incremental Control Allocation (INCA) framework in the context of in-flight optimization of arbitrary secondary flight control design objectives. An extension to the existing INCA concept is formulated that isolates this secondary control task from generating primary control demands. Moreover, an alternative, but closely related design method based on optimal control principles is proposed that extents the role of the control allocator to active control of the system dynamics. Design examples are demonstrated for least-squares minimization of total drag and control activity. These are analyzed in linear and nonlinear simulation scenarios based on an open-source General Dynamics F-16 simulation model.

I. Introduction

Operational mission profile and in-service performance levels of an aircraft are driving factors that determine the functional architecture of flight control systems (FCS). Meeting all requirements related to safety, flying quality, and ride comfort can be seen as the primary FCS design objective. The flight condition-dependent nature of the aerodynamics of the airframe and the available control authority implies that diverse control strategies may be required to meet these design goals. The consequence is that the FCS functional architecture may consist of a large number of control effectors. Distributed roll mechanisms such as in-board/out-board ailerons and roll spoilers [1] are common examples, as are high-lift devices such as flaps and slats. More extensive and complex system architectures are seen in case of extreme maneuvering capabilities and high angle-of-attack flight. For such capabilities, additional mechanisms such as leading edge flaps or thrust vectoring functionality [2, 3] may be required. Another example is the case of Vertical Take-off or Landing (VTOL), which can be achieved by installing e.g. lifting fans [4] or tilting rotors [5].

In addition to meeting these primary design goals, modern flight control systems may be configured to improve secondary performance objectives as well. These can for example refer to aerodynamic and structural efficiency of the airframe, but also other performance features such as energy consumption [6]. Recent civil transport production aircraft reflect an increasing relevance of this aspect. For example, the Airbus A350XWB features an adaptive dropped hinge flap to enhance aerodynamic performance of the main wing during the cruise phase [7]. Likewise, the Boeing 787 family features a Trailing Edge Variable Camber (TEVC) system for a similar purpose [8]. These techniques can be seen as examples of multi-functional effector suites, which enable further functional integration of the flight control system [7].

Control allocation (CA) methods can be adopted to make adequate use of the available control effector suite during every flight phase of the mission profile. In case the control problem is over-determined, the control design can be configured such that the additional degrees of freedom are exploited to meet secondary design goals. To this end, optimal effector configurations shall ideally be established during both trim and off-trim flight conditions. A significant number of different control allocation techniques have been studied in the past, such as direct allocation [9], daisy chaining [10], and redistributed pseudo-inverse [11]. Taking an overhead view, a distinction can be made between linear and non-linear allocation methods [11] as well as frame-wise strategies [6]. This last category takes into account the effector rate limitations by calculating incremental position changes at every time-step (frame) of the flight control computer. Moreover, it enables the use of local control effectiveness models to increase the accuracy of the control

---

[*] Ph.D. Student, Control and Simulation Division, Faculty of Aerospace Engineering, Kluyverweg 1, 2629HS Delft, the Netherlands
[†] Assistant Professor, Control and Simulation Division, Faculty of Aerospace Engineering, Kluyverweg 1, 2629HS Delft, the Netherlands

allocation module in case of nonlinear effector models. This strategy also appears in the literature as Incremental Nonlinear Control Allocation (INCA), which aims at mitigating some of the inherent limitations of conventional control allocation methods when applied to coupled, nonlinear control problems [12].

Many of these techniques focus mainly on allocating manoeuvre commands generated by a high-level primary control law. By contrast, the question of optimality in terms of the secondary control objectives is often given relatively little attention. This is reflected by the fact that this part of the design is often approached by scheduling a desired or preferred (stationary) position for each effector as a function of flight phase [4]. More advanced methods typically perform on-line optimization to impose on-line control constraints [13] or to minimize effector-induced performance losses [6, 14]. However, limiting the optimization to effector-induced losses only may not always be appropriate. For example, seeking effector configurations that minimize the aerodynamic drag generated by the control surfaces may not automatically result in minimum drag of the overall airframe. This naturally leads to the question how a control allocation scheme can be configured that produces overall minimum drag control solutions.

This optimality question forms the main scope of this work. It will be investigated in the context of the Incremental Nonlinear Control Allocation (INCA) framework proposed by [12]. There has been previous research on INCA with additional focus on optimizing effector configurations based on secondary control objectives [15]. However, this study considered the allocation problem as a weighted least squares (WLS) optimization of the primary and secondary control objectives. This introduces an undesirable trade-off between tracking performance and secondary performance optimization, which is unnecessary if the control problem is over-determined. Therefore, in addition to focusing on the optimality question, another goal of this article is to formulate an INCA design that prevents such a trade-off. This must also be viewed as an extension of the study described in [16], where a simple incremental control concept was formulated that minimized the control-induced performance loss of an isolated control effector.

The contribution of this work is threefold. Firstly, the incremental nonlinear *control allocation* (INCA) algorithm is extended to deal with arbitrary secondary objectives in the kernel or null-space of the control effectiveness matrix. Secondly, a closely related kernel-projected incremental *optimal control* law is proposed that enables optimal use of effector redundancy when the secondary control task requires active control of the system state. These items are introduced in Sections II.B and II.C, respectively. Thirdly, performance of the extended INCA concept is evaluated in the context of weighted least squares minimization of airframe drag and control effector activity. The case study that stands at the basis of this assessment is described in Section III. Linear and nonlinear simulation results are discussed in Sections IV and V, respectively. Finally, the article is concluded in Section VI.

II. Fundamentals

The fundamental theory behind the proposed control concepts is formulated in this Section. First, a concise introduction to Incremental Nonlinear Dynamic Inversion (INDI)-based control is given in Subsection II.A. With respect to the multi-objective control architecture, this part of the control law largely serves to fulfill the primary control task. This is followed by a formulation of the extended Incremental Nonlinear Control Allocation (INCA) algorithm in Subsection II.B, which approaches the secondary control task as a static optimization problem within the kernel or null-space of the control effectiveness matrix. This is followed by the description of an alternative, but closely related concept based on nonlinear optimal control in Subsection II.C. This design method effectively extends the traditional scope of control allocation. Finally, Subsection II.D discusses some special forms of the proposed control laws.

A. Incremental Nonlinear Dynamic Inversion

Consider a nonlinear multi-input multi-output (MIMO) system Σ of the form

$$\Sigma : \begin{cases} \dot{\boldsymbol{x}} = \boldsymbol{f}(\boldsymbol{x}) + \boldsymbol{g}(\boldsymbol{x}, \boldsymbol{u}) \\ \boldsymbol{y} = \boldsymbol{h}(\boldsymbol{x}) \end{cases} \tag{1}$$

described by the state vector $\boldsymbol{x} \in \mathbb{R}^n$, the input vector $\boldsymbol{u} \in \mathbb{R}^m$, the observation vector $\boldsymbol{y} \in \mathbb{R}^p$, and smooth mappings $\boldsymbol{f}$, $\boldsymbol{g}$, and $\boldsymbol{h}$. It is assumed throughout this work that $m > p$, which implies that the control system is over-determined. A dynamic inversion control law can be obtained by taking repeated Lie derivatives of the system output until the input vector $\boldsymbol{u}$ appears in the formulation. This can be done for any system relative degree that is nonzero [17]. Assuming for simplicity that the relative degree ρ equals one in all axes, the following description of the output dynamics emerges:

$$\dot{\boldsymbol{y}} = \frac{\partial \boldsymbol{h}}{\partial \boldsymbol{x}} \left(\boldsymbol{f}(\boldsymbol{x}) + \boldsymbol{g}(\boldsymbol{x}, \boldsymbol{u}) \right) \triangleq \boldsymbol{\alpha}(\boldsymbol{x}) + \boldsymbol{\beta}(\boldsymbol{x}, \boldsymbol{u}) \tag{2}$$

This result enables the construction of an incremental nonlinear dynamic inversion (INDI) feedback control law, which can be obtained by taking a Taylor expansion of the output dynamics at the previous timestep $(k-1)$ [17, 18]. Consequently,

$$\dot{\boldsymbol{y}}_k = \dot{\boldsymbol{y}}_{k-1} + \left.\frac{\partial\left[\boldsymbol{\alpha}(\boldsymbol{x}) + \boldsymbol{\beta}(\boldsymbol{x},\boldsymbol{u})\right]}{\partial \boldsymbol{x}}\right|_{k-1} \underbrace{(\boldsymbol{x}_k - \boldsymbol{x}_{k-1})}_{\Delta \boldsymbol{x}_k} + \left.\frac{\partial \boldsymbol{\beta}(\boldsymbol{x},\boldsymbol{u})}{\partial \boldsymbol{u}}\right|_{k-1} \underbrace{(\boldsymbol{u}_k - \boldsymbol{u}_{k-1})}_{\Delta \boldsymbol{u}_k} + \boldsymbol{r}_{1,k} \tag{3}$$

In order to arrive at the INDI control law, the time-scale separation principle needs to be applied [17, 19, 20]. This implies that all incremental state-dependent and high-order residual terms can be neglected with respect to the other terms in the Taylor expansion. As a result, the following expression is obtained:

$$\boldsymbol{\tau}_k \triangleq \boldsymbol{\nu}_k - \dot{\boldsymbol{y}}_{k-1} = \mathcal{B}_{k-1}\Delta\boldsymbol{u}_k \tag{4}$$

where $\boldsymbol{\nu}_k \in \mathbb{R}^p$ is the pseudo-control input generated by an auxiliary control loop and $\mathcal{B}_{k-1} = \mathcal{B}(\boldsymbol{x}_{k-1}, \boldsymbol{u}_{k-1}) \triangleq \left.\frac{\partial \boldsymbol{\beta}(\boldsymbol{x},\boldsymbol{u})}{\partial \boldsymbol{u}}\right|_{k-1}$ represents the control effectiveness matrix. This result forms an equality constraint that is to be satisfied by the control allocation module.

B. Incremental Control Allocation with Kernel Restoring

Based on this understanding, the incremental nonlinear control allocation (INCA) problem can be defined as the following constrained static optimization problem in the case $m > p$:

$$\min_{\boldsymbol{u}_k \in \mathcal{U}} L(\boldsymbol{x}_k, \boldsymbol{u}_k) \quad \text{subject to} \quad \mathcal{B}_{k-1}\Delta\boldsymbol{u}_k = \boldsymbol{\tau}_k \tag{5}$$

where $L \geq 0 \in \mathbb{R}$ represents a scalar objective function that shall be minimized by an admissible control vector $\boldsymbol{u}_k \in \mathcal{U} \subset \mathbb{R}^m$ for the system state $\boldsymbol{x}_k$. In what follows, the question of how to deal with input limits will not be further considered; these can be accounted for using e.g. interior-point methods [21] or a redistribution procedure [11] as described in Subsection V.A.2. Consequently, the original problem can be transformed into a Lagrangian formulation by introducing a Lagrange multiplier $\boldsymbol{\lambda} \in \mathbb{R}^m$,

$$\mathcal{L}(\boldsymbol{x}_k, \boldsymbol{u}_k, \boldsymbol{\lambda}_k) = L(\boldsymbol{x}_k, \boldsymbol{u}_k) + \boldsymbol{\lambda}_k^T(\boldsymbol{\tau}_k - \mathcal{B}_{k-1}\Delta\boldsymbol{u}_k) \tag{6}$$

Using the fact that $\Delta\boldsymbol{u}_k \triangleq \boldsymbol{u}_k - \boldsymbol{u}_{k-1}$, optimality is achieved when

$$\frac{\partial \mathcal{L}}{\partial \boldsymbol{u}_k} = \frac{\partial L(\boldsymbol{x}_k, \boldsymbol{u}_k)}{\partial \boldsymbol{u}_k} - \boldsymbol{\lambda}_k^T \mathcal{B}_{k-1} = \boldsymbol{0} \tag{7}$$

$$\frac{\partial \mathcal{L}}{\partial \boldsymbol{\lambda}_k} = \boldsymbol{\tau}_k - \mathcal{B}_{k-1}\Delta\boldsymbol{u}_k = \boldsymbol{0} \tag{8}$$

Assuming $L(\boldsymbol{x}_k, \boldsymbol{u}_k)$ is twice differentiable in $\boldsymbol{u}_k$, a second-order Taylor expansion can be established to formulate a quadratic approximation of the objective function:

$$L(\boldsymbol{x}_k, \boldsymbol{u}_k) = L(\boldsymbol{x}_k, \boldsymbol{u}_{k-1}) + \nabla_u L(\boldsymbol{x}_k, \boldsymbol{u}_{k-1})^T \Delta\boldsymbol{u}_k + \frac{1}{2}\Delta\boldsymbol{u}_k^T \nabla_{uu}^2 L(\boldsymbol{x}_k, \boldsymbol{u}_{k-1})\Delta\boldsymbol{u}_k + r_{2,k} \tag{9}$$

For completeness, the following incremental delay operator is defined:

$$\begin{cases} \boldsymbol{\eta}_{k+1} = \boldsymbol{\eta}_k + \Delta\boldsymbol{u}_k \\ \boldsymbol{u}_{k-1} = \boldsymbol{\eta}_k \end{cases} \tag{10}$$

which enables the definition of the augmented state vector $z_k = \begin{bmatrix}\boldsymbol{x}_k^T & \boldsymbol{\eta}_k^T\end{bmatrix}^T = \begin{bmatrix}\boldsymbol{x}_k^T & \boldsymbol{u}_{k-1}^T\end{bmatrix}^T$. Consequently, using $\boldsymbol{L}_{\boldsymbol{u},k} = \boldsymbol{L}_u(z_k) \triangleq \nabla_u L(\boldsymbol{x}_k, \boldsymbol{u}_{k-1})^T$ and $R_k = R(z_k) \triangleq \nabla_{uu}^2 L(\boldsymbol{x}_k, \boldsymbol{u}_{k-1})$ and assuming $r_{2,k} \approx 0$, the following control increment is found from Equation 7:

$$\Delta\boldsymbol{u}_k = -R_k^{-1}\left(\boldsymbol{L}_{\boldsymbol{u},k} - \mathcal{B}_{k-1}^T \boldsymbol{\lambda}_k\right) \tag{11}$$

Substituting this expression in Equation 8 yields

$$\boldsymbol{\lambda}_k = \left(\mathcal{B}_{k-1} R_k^{-1} \mathcal{B}_{k-1}^T\right)^{-1} \left(\boldsymbol{\tau}_k + \mathcal{B}_{k-1} R_k^{-1} \boldsymbol{L}_{\boldsymbol{u},k}\right) \tag{12}$$

which in combination with Equation 11 results in the final control law

$$\Delta \boldsymbol{u}_k = P_k \boldsymbol{\tau}_k - N_k R_k^{-1} \boldsymbol{L}_{\boldsymbol{u},k} \triangleq \Delta \bar{\boldsymbol{u}}_k + \Delta \boldsymbol{u}_k^{\perp} \tag{13}$$

where

$$P_k = \mathcal{B}_k^{+} \triangleq R_k^{-1} \mathcal{B}_{k-1}^T \left(\mathcal{B}_{k-1} R_k^{-1} \mathcal{B}_{k-1}^T\right)^{-1} \tag{14}$$

$$N_k = \mathcal{B}_k^{\perp} \triangleq I - P_k \mathcal{B}_{k-1} \tag{15}$$

The resulting INCA law can be viewed as an online variant of a constrained sequential quadratic programming (SQP) optimizer [11, 21] that performs one iteration per time step. It consists of two parts. The first element $\Delta \bar{\boldsymbol{u}}_k$ can be recognized as the primary incremental control input, which ensures that incremental control demands are allocated in a least-squares fashion over the control effector suite. The second element $\Delta \boldsymbol{u}_k^{\perp}$ can be seen as the restoring element [6], which optimizes the effector configuration according to the secondary control objective. The restoring input remains within the kernel or null-space of $\mathcal{B}$ and does therefore not affect the tracking performance of the incremental control law. This INCA scheme features close similarities to existing nonlinear control allocation approaches [11].

C. Kernel-projected Incremental Optimal Control

The driving philosophy behind control allocation is to isolate the effector distribution task from the motion control law [22]. However, this concept is generally too restrictive when both primary and secondary control objectives require active control of the system dynamics. If this is the case, the focus of the control distribution task shifts from *static* control allocation to *dynamic* optimal control. Nevertheless, it will be shown in this Section that there are significant similarities between these two strategies. First, the static optimization problem formulated in Equation 5 needs to be converted to a dynamic alternative. Given the incremental nature of the control law, this is done based on a discrete-time formulation of the optimal control problem [23] in combination with the INDI equality constraint:

$$\min_{\boldsymbol{u} \in \mathcal{U}} \lim_{N \to \infty} \sum_{k=i}^{N} L(\boldsymbol{x}_k, \boldsymbol{u}_k) \quad \text{subject to} \quad \mathcal{B}_{k-1} \Delta \boldsymbol{u}_k = \boldsymbol{\tau}_k \tag{16}$$

Accordingly, the sampled-data representation of the system Σ describing the open-loop plant will be used:

$$\bar{\Sigma} : \begin{cases} \boldsymbol{x}_{k+1} = \bar{\boldsymbol{f}}(\boldsymbol{x}_k) + \bar{\boldsymbol{g}}(\boldsymbol{x}_k, \boldsymbol{u}_k) \\ \boldsymbol{y}_k = \boldsymbol{h}(\boldsymbol{x}_k) \end{cases} \tag{17}$$

In order to arrive at the kernel-projected optimal control, a Hamiltonian function needs to be constructed that incorporates the static Langrangian formulation from Equation 6. Before doing so, the incremental nature of the control law demands the introduction of the one-step delayed input vector as an additional state in the optimal control formulation. Using the incremental delay operator defined by Equation 10 and performing the necessary algebraic manipulations in Equations 17 and 10, the augmented system dynamics are described by the following compact difference equation:

$$z_{k+1} = \boldsymbol{f}^*(z_k, \Delta \boldsymbol{u}_k) \tag{18}$$

This yields the necessary ingredients to construct the Hamiltonian, which is defined as follows:

$$\mathcal{H}(\boldsymbol{x}_k, \boldsymbol{u}_k, \boldsymbol{u}_{k-1}, \Delta \boldsymbol{u}_k, \boldsymbol{\lambda}_k, \tilde{\boldsymbol{\lambda}}_{k+1}) = L(\boldsymbol{x}_k, \boldsymbol{u}_k) + \boldsymbol{\lambda}_k^T (\boldsymbol{\tau}_k - \mathcal{B}_{k-1} \Delta \boldsymbol{u}_k) + \tilde{\boldsymbol{\lambda}}_{k+1}^T \boldsymbol{f}_*(\boldsymbol{x}_k, \boldsymbol{u}_{k-1}, \Delta \boldsymbol{u}_k) \tag{19}$$

Incorporating the Taylor expansions for $L(\boldsymbol{x}_k, \boldsymbol{u}_k)$ and $\bar{\boldsymbol{g}}(\boldsymbol{x}_k, \boldsymbol{u}_k)$, recognizing that $\boldsymbol{u}_k = \boldsymbol{u}_{k-1} + \Delta \boldsymbol{u}_k$, and substituting $z_k = \begin{bmatrix} \boldsymbol{x}_k^T & \boldsymbol{u}_{k-1}^T \end{bmatrix}^T$ results in the following expression:

$$\begin{aligned} \mathcal{H}(z_k, \Delta \boldsymbol{u}_k, \boldsymbol{\lambda}_k, \tilde{\boldsymbol{\lambda}}_{k+1}) = L(z_k) + \boldsymbol{L}_{\boldsymbol{u},k} \Delta \boldsymbol{u}_k + \frac{1}{2} \Delta \boldsymbol{u}_k^T R_k \Delta \boldsymbol{u}_k + \boldsymbol{\lambda}_k^T (\boldsymbol{\tau}_k - \mathcal{B}_{k-1} \Delta \boldsymbol{u}_k) + \\ \tilde{\boldsymbol{\lambda}}_{k+1}^T \left(\boldsymbol{f}^*(z_k, \boldsymbol{0}) + G^*(z_k, \boldsymbol{0}) \Delta \boldsymbol{u}_k\right) \end{aligned} \tag{20}$$

Here, $G^*(\bullet)$ represents the augmented control effectiveness matrix. The optimal incremental control $\Delta \boldsymbol{u}_k$ should minimize $\mathcal{H}(\bullet)$ while ensuring that the equality constraints that arise from the primary control objective are met. This can be achieved by applying the optimality conditions from Equations 7 and 8 to the Hamiltonian. For the present problem formulation, this approach is equivalent to applying Pontryagin's Minimum Principle [23] after establishing the optimal form of the static Lagrange multiplier. The latter is found as

$$\lambda_k = \left(\mathcal{B}_{k-1} R_k^{-1} \mathcal{B}_{k-1}^T\right)^{-1} \left(\boldsymbol{\tau}_k + \mathcal{B}_{k-1} R_k^{-1} \boldsymbol{L}_{\boldsymbol{u},k} + \mathcal{B}_{k-1} R_k^{-1} {G_k^*}^T \tilde{\boldsymbol{\lambda}}_{k+1}\right) \tag{21}$$

where $G_k^* = G^*(z_k, \boldsymbol{0})$. Likewise, the stationarity condition leads to

$$\Delta \boldsymbol{u}_k = -R_k^{-1} \boldsymbol{L}_{\boldsymbol{u},k} - R_k^{-1} {G_k^*}^T \tilde{\boldsymbol{\lambda}}_{k+1} + R_k^{-1} \mathcal{B}_{k-1}^T \lambda_k \tag{22}$$

Consequently, using P_k and N_k as described by Equations 14 and 15 and substituting Equation 21 into 22 yields the optimal control law

$$\Delta \boldsymbol{u}_k = P_k \boldsymbol{\tau}_k - N_k R_k^{-1} \left(\boldsymbol{L}_{\boldsymbol{u},k} + {G_k^*}^T \tilde{\boldsymbol{\lambda}}_{k+1}\right) \triangleq \Delta \bar{\boldsymbol{u}}_k + \Delta \boldsymbol{u}_k^{\perp} \tag{23}$$

Comparing the above expression to the static INCA law from Equation 13 shows significant similarities. It is observed that additional knowledge of the future costate vector $\tilde{\boldsymbol{\lambda}}_{k+1}$ is needed to convert the static control allocation mapping to a dynamically optimal control law. Therefore, the control law in Equation 23 transcends the traditional scope of utilizing effector redundancy in dynamic inversion control architectures.

D. ℓ_2-norm Performance Optimization with Time-Scale Separation Simplification

As an important special case, the following formulation of the objective function L is considered:

$$L(\boldsymbol{x}_k, \boldsymbol{u}_k, \Delta \boldsymbol{u}_k) = \frac{1}{2} \|\boldsymbol{\sigma}_k\|_2^2 + \frac{1}{2} \Delta \boldsymbol{u}_k^T W_r \Delta \boldsymbol{u}_k \tag{24}$$

which corresponds to minimizing the ℓ_2-norm of a linear system performance function output $\boldsymbol{\sigma}_k = \boldsymbol{\zeta}(\boldsymbol{x}_k, \boldsymbol{u}_k)$ with additional penalties on control increments. The latter can be viewed as a way to penalize effector rates and has been adopted before in existing literature [24]. Denoting the gradient of $\boldsymbol{\zeta}(\bullet)$ with respect to $\boldsymbol{u}_k$ as $\Upsilon(\bullet)$ yields the following expression for the *static* INCA law:

$$\Delta \boldsymbol{u} = P_k \boldsymbol{\tau}_k - N_k R_k^{-1} \Upsilon_k^T \boldsymbol{\zeta}_k \tag{25}$$

where $R_k = \Upsilon_k^T \Upsilon_k + W_r$. Likewise, the *dynamic* optimal control law reads as:

$$\Delta \boldsymbol{u} = P_k \boldsymbol{\tau}_k - N_k R_k^{-1} \left(\Upsilon_k^T \boldsymbol{\zeta}_k + {G_k^*}^T \tilde{\boldsymbol{\lambda}}_{k+1}\right) \tag{26}$$

The consequence of the selected notation (subscript k) must be emphasized, as it masks the dependency on the augmented state vector z_k. In the context of the performance output vector for example, it holds that $\boldsymbol{\zeta}_k = \boldsymbol{\zeta}(z_k) = \boldsymbol{\zeta}(\boldsymbol{x}_k, \boldsymbol{u}_{k-1})$. Therefore, information from two different time steps needs to be incorporated. This is problematic in case one would like to use direct measurements of the performance output instead. It is recognized that this issue can be largely circumvented if the time-scale separation (TSS) principle that is commonly used in the derivation of sensor-based INDI control laws holds for $\boldsymbol{\zeta}(\boldsymbol{x}_k, \boldsymbol{u}_k)$ as well. In that case, one can simplify according to:

$$\boldsymbol{\zeta}_k \approx \boldsymbol{\zeta}(\boldsymbol{x}_{k-1}, \boldsymbol{u}_{k-1}) + \left.\frac{\partial \boldsymbol{\zeta}(\boldsymbol{x}_k, \boldsymbol{u}_{k-1})}{\partial \boldsymbol{x}_k}\right|_{k-1} \underbrace{(\boldsymbol{x}_k - \boldsymbol{x}_{k-1})}_{\Delta \boldsymbol{x}_k \approx \boldsymbol{0}} \approx \boldsymbol{\sigma}_{k-1} \tag{27}$$

This enables the direct incorporation of measurements in the static INCA law from Equation 25, which results in the simplified control law

$$\Delta \boldsymbol{u} = P_k \boldsymbol{\tau}_k - N_k R_k^{-1} \Upsilon_k^T \boldsymbol{\sigma}_{k-1} \tag{28}$$

For the dynamic optimal control law, the TSS simplification must be applied *after* the optimal costate trajectory has been determined. Consequently, the TSS-simplified dynamic optimal control that optimizes the ℓ_2-norm of the performance output is readily found as

$$\Delta \boldsymbol{u} = P_k \boldsymbol{\tau}_k - N_k R_k^{-1} \left(\Upsilon_k^T \boldsymbol{\sigma}_{k-1} + {G_k^*}^T \tilde{\boldsymbol{\lambda}}_{k+1}\right) \tag{29}$$

III. Design Case Study Description

This section briefly introduces the control design case study for which a multi-objective control law is to be designed and analyzed. The simulation model is discussed first in Subsection III.A, which is followed by an outline of the INDI-based primary flight control law design in Subsection III.B. The secondary performance objective is briefly described in Subsection III.C. Subsequent development of the kernel-projected part of the control law is discussed later in Section IV.

A. Bare airframe description

In order to demonstrate its abilities on an exemplary control allocation task, the proposed INCA-R scheme is applied to a dynamic inversion control law design for an open-source nonlinear simulation model of the General Dynamics F-16 aircraft [25, 26]. The active aerodynamic control effector suite consists of a symmetric horizontal tail, flaperons, rudder, and leading edge flap (LEF). It should be remarked that the existing F-16 flight control system design philosophy does not consider the LEF part of the active set, as it is scheduled with angle of attack and dynamic pressure to maximize the lift/drag ratio and improve directional stability at high angle-of-attack [27]. The aerodynamic database was established based on low-speed static and dynamic (forced-oscillation) wind-tunnel test data from a sub-scale model and covers an angle-of-attack and angle-of-sideslip range of $-20° \leq \alpha \leq +60°$ and $|\beta| \leq 30°$, respectively. The longitudinal force and moment coefficients can be found below; a description of the full aerodynamic database is available in [25].

$$C_{X,t} = C_X(\alpha,\beta,\delta_h) + \Delta C_{X_{LEF}}\left(1-\frac{\delta_{LEF}}{\delta_{LEF,max}}\right) + \frac{\bar{c}q}{2V}\left[C_{X_q}(\alpha) + \Delta C_{X_{q_{LEF}}}(\alpha)\left(1-\frac{\delta_{LEF}}{\delta_{LEF,max}}\right)\right] \tag{30}$$

$$C_{Z,t} = C_Z(\alpha,\beta,\delta_h) + \Delta C_{Z_{LEF}}\left(1-\frac{\delta_{LEF}}{\delta_{LEF,max}}\right) + \frac{\bar{c}q}{2V}\left[C_{Z_q}(\alpha) + \Delta C_{Z_{q_{LEF}}}(\alpha)\left(1-\frac{\delta_{LEF}}{\delta_{LEF,max}}\right)\right] \tag{31}$$

$$\begin{aligned} C_{m,t} = {} & C_m(\alpha,\beta,\delta_h)\eta_{\delta_h}(\delta_h) + C_{Z,t}(x_{CG,ref} - x_{CG}) + \Delta C_{m_{LEF}}\left(1-\frac{\delta_{LEF}}{\delta_{LEF,max}}\right) \\ & + \frac{\bar{c}q}{2V}\left[C_{m_q}(\alpha) + \Delta C_{m_{q,LEF}}(\alpha)\left(1-\frac{\delta_{LEF}}{\delta_{LEF,max}}\right)\right] + \Delta C_m(\alpha) \end{aligned} \tag{32}$$

where

$$\Delta C_{(.)_{LEF}} \triangleq \Delta C_{(.)_{LEF}}(\alpha,\beta) - \Delta C_{(.)}(\alpha,\beta,\delta_h = 0) \tag{33}$$

and δ_h and δ_{LEF} represent the horizontal tail and leading edge flap (LEF) control surface positions, respectively. These are both driven by actuators that are modeled as a first-order lag with time constants of 0.0495 and 0.136 seconds, respectively. Moreover, x_{CG} represents the longitudinal center of gravity (CG) position in terms of %MAC, and $\eta_{\delta_h}(\delta_h) = 1$ for the deflection ranges encountered in this study.

B. Primary flight control law design

The control law is selected as an angular rate demand design that consists of an outer linear two degree-of-freedom (2DOF) proportional-integral (PI) controller wrapped around an incremental nonlinear dynamic inversion (INDI) inner loop. Figure 1 shows a block diagram of the full control system. For a rate response type, angular acceleration forms a natural command variable (CV) that is to be inverted by the INDI loop. In this view, the INDI control law can be derived starting from the rotational equations of motion in the body frame:

$$\dot{\boldsymbol{\omega}} = \boldsymbol{J}^{-1}\left(\boldsymbol{M}(\boldsymbol{x},\boldsymbol{u}) - \boldsymbol{\omega}\times\boldsymbol{J}\boldsymbol{\omega}\right) \tag{34}$$

Since the input arises directly, this equation can be used immediately for dynamic inversion. Taking the Taylor expansion around the current time-step t_0 yields the following formulation:

$$\begin{aligned} \dot{\boldsymbol{\omega}} = \dot{\boldsymbol{\omega}}_0 & + \frac{\partial}{\partial \boldsymbol{x}}\left[\boldsymbol{J}^{-1}\left(\boldsymbol{M}(\boldsymbol{x},\boldsymbol{u}) - \boldsymbol{\omega}\times\boldsymbol{J}\boldsymbol{\omega}\right)\right]\Delta\boldsymbol{x} + \frac{\partial}{\partial \boldsymbol{\delta}}\left[\boldsymbol{J}^{-1}\left(\boldsymbol{M}(\boldsymbol{x},\boldsymbol{u}) - \boldsymbol{\omega}\times\boldsymbol{J}\boldsymbol{\omega}\right)\right]\Delta\boldsymbol{\delta} \\ & + \frac{\partial}{\partial \delta_{LEF}}\left[\boldsymbol{J}^{-1}\left(\boldsymbol{M}(\boldsymbol{x},\boldsymbol{u}) - \boldsymbol{\omega}\times\boldsymbol{J}\boldsymbol{\omega}\right)\right]\Delta\delta_{LEF} + \boldsymbol{R}_1 \end{aligned} \tag{35}$$

Working out the partial derivatives, applying the time-scale separation principle, and isolating the longitudinal dynamics results in the following incremental control law:

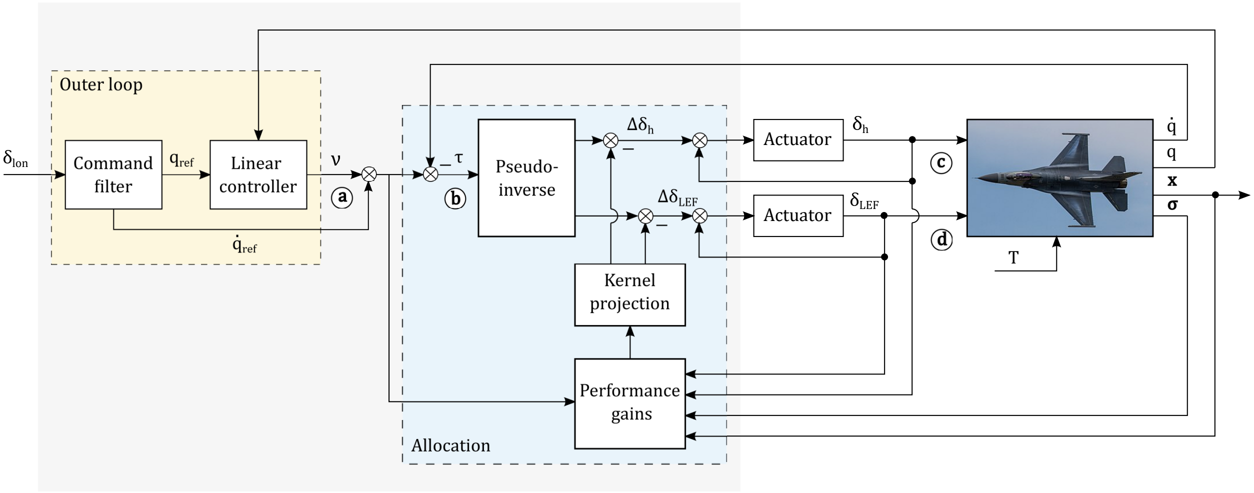

Fig. 1 Control system overview

$$\tau_k = \begin{bmatrix} \hat{M}_{\delta_h}(\boldsymbol{x}_k, \boldsymbol{u}_{k-1})J_{yy} & \hat{M}_{\delta_{LEF}}(\boldsymbol{x}_k, \boldsymbol{u}_{k-1})J_{yy} \end{bmatrix} \begin{bmatrix} \Delta\delta_{h,k} \\ \Delta\delta_{LEF,k} \end{bmatrix} \triangleq \mathcal{B}(\boldsymbol{x}_k, \boldsymbol{u}_{k-1})\Delta\boldsymbol{u}_k \tag{36}$$

where $\tau_k \triangleq \nu_k - \dot{q}_{k-1}$. The pseudo-control ν is generated according to the control law

$$\nu = \dot{q}_{ref} + K_P\left(q_{ref} - q\right) \tag{37}$$

For all designs described in this work, a proportional gain of $K_P = 5$ is used. The desired angular rates to control inceptor input are obtained through the following command filter:

$$\frac{q_{ref}(s)}{\delta_{lon}(s)} = \frac{K_q(T_{\theta_2}s + 1)}{s^2 + 2\zeta_{sp}\omega_{sp}s + \omega_{sp}^2} \tag{38}$$

This command filter is consistent with the desired Low Equivalent System (LOES) response profiles suggested in [28]. The design parameters are selected as $K_q = 3.4\omega_{sp}^2$, $T_{\theta_2} = 1.0$ seconds, $\zeta_{sp} = 1.0$, and $\omega_{sp} = 4.0$ rad/s. Lastly, the INDI loop is run at 100 Hz.

C. Secondary performance objective

Multi-functional flight control law designs may exploit advanced objectives in the the control surface positioning logic. Online sensor information could be used that directly translate these objectives to real-time control solutions. The online strategy suggested here aims to minimize a least-squares weighted combination of the airframe's total drag coefficient and effector control activity. The following objective function definition is adopted to this end:

$$L(\boldsymbol{x}, \boldsymbol{u}) = \left(\frac{C_{D,k}}{C_{D_{ref}}}\right)^2 + \frac{1}{2}\boldsymbol{u}_k^T W_p \boldsymbol{u}_k + \frac{1}{2}\Delta\boldsymbol{u}_k^T W_r \Delta\boldsymbol{u}_k \tag{39}$$

Here, $C_{D_{ref}}$ is introduced to normalize the drag coefficient with respect to the control activity terms. Accordingly, the performance output and Hessian functions are given as:

$$\boldsymbol{\sigma}_k = diag\left(\frac{1}{C_{D_{ref}}}, W_p^{1/2}\right)\begin{bmatrix} C_{D_k} \\ \boldsymbol{u}_k \end{bmatrix}, \qquad R_k = \frac{1}{C_{D_{ref}}^2}\boldsymbol{C}_{\boldsymbol{D_u}k}^T \boldsymbol{C}_{\boldsymbol{D_u}k} + W_p + W_r \tag{40}$$

Contrary to an objective function that would only include effector-related terms, the fact that the drag-related term needs to be estimated on-line introduces an inherent level of uncertainty. Since the objective functions effectively consists of a combination of two sub-objectives, this implies that the relative weighting of these terms may be different in the presence of uncertainty. However, this aspect will not be further considered.

IV. Linear Design and Analysis

Control allocation techniques become especially relevant in a nonlinear context, as these may exploit the nonlinear nature of the control problem to seek (global) minima where that the control-induced performance is minimized at every timestep. However, it is of high interest to first conduct performance analysis in a linear context. The foremost reason is that this enables straightforward verification of the multi-objective control design from the perspective of the true optimal control solution. Moreover, the kernel-projected infinite-horizon optimal control law can be derived in analytical form. The incremental control allocation and kernel-projected optimal control designs are both described in Subsection IV.A. Nominal and robust performance are discussed in subsequent subsections. The effects of these control strategies on stability margins are considered as well.

A. Multi-objective Incremental Control Law Construction

Consider the MIMO system Σ in linear form with inversion variable $\boldsymbol{y}$ and performance vector $\boldsymbol{\sigma}$ as follows

$$\Sigma : \begin{cases} \dot{\boldsymbol{x}} = A\boldsymbol{x} + B\boldsymbol{u} \\ \boldsymbol{y} = C_y\boldsymbol{x} \\ \boldsymbol{\sigma} = C_\sigma\boldsymbol{x} + D_\sigma\boldsymbol{u} \end{cases} \tag{41}$$

A key insight to arrive at the optimal restoring control law is that the optimal control *after* closing the primary control loop must be found. Using the primary control loop design described in the previous section, the following expression is found for the incremental control demand:

$$\boldsymbol{\tau} = \boldsymbol{\nu} - \hat{\dot{\boldsymbol{y}}} = \boldsymbol{r} - K_p\boldsymbol{y} - \hat{\dot{\boldsymbol{y}}} = \boldsymbol{r} - K_pC_y\boldsymbol{x} - C_yA\boldsymbol{x} - C_yB\boldsymbol{u}_{k-1} \triangleq \boldsymbol{r} - T\boldsymbol{x} - C_yB\boldsymbol{u}_{k-1} \tag{42}$$

Which leads to the combined control law

$$\boldsymbol{u} = P\boldsymbol{\tau} + \Delta\boldsymbol{u}_k^\perp + \boldsymbol{u}_{k-1} = P\boldsymbol{r} - PT\boldsymbol{x} - PC_yB\boldsymbol{u}_{k-1} + \Delta\boldsymbol{u}_k^\perp + \boldsymbol{u}_{k-1} = P\boldsymbol{r} - PT\boldsymbol{x} + \Delta\boldsymbol{u}_k^\perp + N\boldsymbol{u}_{k-1} \tag{43}$$

where the control effectiveness C_yB is used in the formulation of P in accordance with Equation 14. This results in the following description of the closed-loop system dynamics:

$$\dot{\boldsymbol{x}} = (A - BPT)\,\boldsymbol{x} + B\left(N\boldsymbol{u}_{k-1} + \Delta\boldsymbol{u}_k^\perp\right) \triangleq A_c\boldsymbol{x} + B\boldsymbol{u}^\perp + BP\boldsymbol{r} \tag{44}$$

At this point, a sampled-data representation of the closed-loop system needs to be generated. Doing so yields the following discrete-time description:

$$\boldsymbol{x}_{k+1} = \bar{A}_c\boldsymbol{x}_k + \bar{B}\boldsymbol{u}_k^\perp + \bar{B}P\boldsymbol{r}_k \tag{45}$$

Subsequently, this result can be used to construct the augmented system dynamics:

$$\boldsymbol{z}_{k+1} = \begin{bmatrix} \bar{A}_c & \bar{B}N \\ -PT & N \end{bmatrix}\boldsymbol{z}_k + \begin{bmatrix} \bar{B} \\ \boldsymbol{I} \end{bmatrix}\Delta\boldsymbol{u}_k^\perp + \begin{bmatrix} \bar{B} \\ \boldsymbol{I} \end{bmatrix}P\boldsymbol{r}_k \triangleq A_{c_*}\boldsymbol{z}_k + B_*\Delta\boldsymbol{u}_k^\perp + B_*P\boldsymbol{r}_k \tag{46}$$

with the corresponding optimal orthogonal incremental input terms law described as

$$\Delta\boldsymbol{u}_k^\perp = -NR^{-1}\left(D_\sigma^TV_\sigma\boldsymbol{z}_k + B_*^T\tilde{\lambda}_{k+1}\right) \tag{47}$$

where $V_\sigma \triangleq \begin{bmatrix} C_\sigma & D_\sigma \end{bmatrix}$. Consequently, the closed-loop performance output is derived as

$$\boldsymbol{\sigma}_k = \begin{bmatrix} C_\sigma - D_\sigma PT & D_\sigma N \end{bmatrix}\boldsymbol{z}_k + D_\sigma\left(P\boldsymbol{r}_k + \Delta\boldsymbol{u}_k^\perp\right) \triangleq Y_\sigma\boldsymbol{z}_k + D_\sigma P\boldsymbol{r}_k + D_\sigma\Delta\boldsymbol{u}_k^\perp \tag{48}$$

1. Incremental Control Allocation with Kernel Restoring

The incremental control allocation scheme can be readily obtained from the information in Section II.D. Using the TSS simplification therefore results in the following incremental control input:

$$\Delta\boldsymbol{u}_k = P\boldsymbol{\tau}_k - NR^{-1}D_\sigma^T\boldsymbol{\sigma}_{k-1} \tag{49}$$

In what follows, this will be referred to as the *total* incremental control law.

2. *Kernel-projected Incremental Optimal Control Law*

The system described by Equations 46-48 can be used to construct the optimal secondary control law. This requires the solution S that satisfies the algebraic Riccati equation

$$A_{c_*}^T S A_{c_*} - S - \left(A_{c_*}^T + G\right) S B_* \tilde{R}^{-1} N R^{-1} \left(D_\sigma^T V_\sigma + B_*^T S A_{c_*}\right) + G S A_{c_*} + H = 0 \tag{50}$$

where

$$\begin{aligned} G &= -\left(Y_\sigma^T D_\sigma - T_*^T P^T W_r\right) N R^{-1} B_*^T \\ H &= Y_\sigma^T Y_\sigma + T_*^T P^T W_r P T_* - \left(Y_\sigma^T D_\sigma - T_*^T P^T W_r\right) N R^{-1} D_\sigma^T V_\sigma \end{aligned} \tag{51}$$

as well as a description of the effect of the reference signal on the costate variable. Here, $T_* \triangleq \begin{bmatrix} T & C_y B \end{bmatrix}$. The corresponding derivations have been included in the Appendix. The resulting optimal total incremental control law reads as:

$$\Delta \boldsymbol{u}_k = P \boldsymbol{\tau}_k - \tilde{R}^{-1} N R^{-1} \left(K_z \boldsymbol{z}_k + K_r P \boldsymbol{r}_k\right) \tag{52}$$

where $\tilde{R} \triangleq I + N R^{-1} B_*^T S B_*$ and

$$\begin{aligned} K_z &= D_\sigma^T V_\sigma + B_*^T S A_{c_*} \\ K_r &= B_*^T \left(S B_* + V^{-1} U\right) \\ U &= Y_\sigma^T D_\sigma - T_*^T P^T W_r + \left(A_{c_*}^T + G\right) S B_* \left(I - \tilde{R}^{-1} N R^{-1} B_*^T S B_*\right) \\ V &= I - \left(A_{c_*}^T + G\right) \left(I - S B_* \tilde{R}^{-1} N R^{-1} B_*^T\right) \end{aligned} \tag{53}$$

It must be noted that $C_y B \tilde{R} = C_y B$, which implies $C_y B \tilde{R}^{-1} = C_y B$. Hence the kernel projection property of the secondary control is maintained. Accordingly, applying the TSS simplification results in the following total optimal incremental control law:

$$\Delta \boldsymbol{u}_k = P \boldsymbol{\tau}_k - \tilde{R}^{-1} N R^{-1} \left(D_\sigma^T \boldsymbol{\sigma}_{k-1} + B_*^T S A_{c_*} \boldsymbol{z}_k + K_r P \boldsymbol{r}_k\right) \tag{54}$$

B. Nominal Performance

The control laws are evaluated based on a linear short-period representation of the bare airframe obtained at two different flight conditions. Therefore, the open-loop plant dynamics are governed by the following equations of motion:

$$\begin{aligned} \begin{bmatrix} \dot{\alpha} \\ \dot{q} \end{bmatrix} &= \begin{bmatrix} z_\alpha & z_q \\ m_\alpha & m_q \end{bmatrix} \begin{bmatrix} \alpha \\ q \end{bmatrix} + \begin{bmatrix} z_{\delta_h} & z_{\delta_{LEF}} \\ m_{\delta_h} & m_{\delta_{LEF}} \end{bmatrix} \begin{bmatrix} \delta_h \\ \delta_{LEF} \end{bmatrix}, \qquad y = \begin{bmatrix} 0 & 1 \end{bmatrix} \begin{bmatrix} \alpha \\ q \end{bmatrix} \\ \boldsymbol{\sigma} &= diag(C_{D_{ref}}, W_p^{1/2}) \left(\begin{bmatrix} C_{D_\alpha} & C_{D_q} \\ 0 & 0 \\ 0 & 0 \end{bmatrix} \begin{bmatrix} \alpha \\ q \end{bmatrix} + \begin{bmatrix} C_{D_{\delta_h}} & C_{D_{\delta_{LEF}}} \\ 1 & 0 \\ 0 & 1 \end{bmatrix} \begin{bmatrix} \delta_h \\ \delta_{LEF} \end{bmatrix} \right) \end{aligned} \tag{55}$$

It must be noted that z_{δ_h} and $z_{\delta_{LEF}}$ are responsible for the dynamic coupling in the secondary control task. It is assumed in this analysis that perfect estimates of the drag coefficient are available. The selected flight conditions both correspond to straight-and-level flight. Moreover, the C.G. is located at 38% relative to the mean aerodynamic chord (MAC), which results in a statically unstable airframe. The reason for using the short-period reduced form is that steady-state performance can be assessed in a straightforward fashion. The control law design parameters are selected as $C_{D_{ref}} = 0.01$, $W_p^{1/2} = 5diag(\frac{1}{\overline{\delta}_h - \underline{\delta}_h}, \frac{1}{\overline{\delta}_{LEF} - \underline{\delta}_{LEF}})$, and $W_r = 0.25diag(0.1, 1)$. Here, the effector limits $[\underline{\delta}_h, \overline{\delta}_h] = [-25, 25]$ and $[\underline{\delta}_{LEF}, \overline{\delta}_{LEF}] = [0, 25]$ are used (in degrees). Figure 2 shows the step response of the control allocation and optimal control designs for the first flight condition (V_0 = 500 ft/s or M0.46, h = 10,000 ft). It is emphasized that the presented variables are with respect to their respective trim values. A benchmark response where the LEF remains in trim position is displayed as well. The incremental control problem becomes exactly determined in this benchmark case, which implies that the control law reduces to a standard incremental dynamic inversion (IDI)

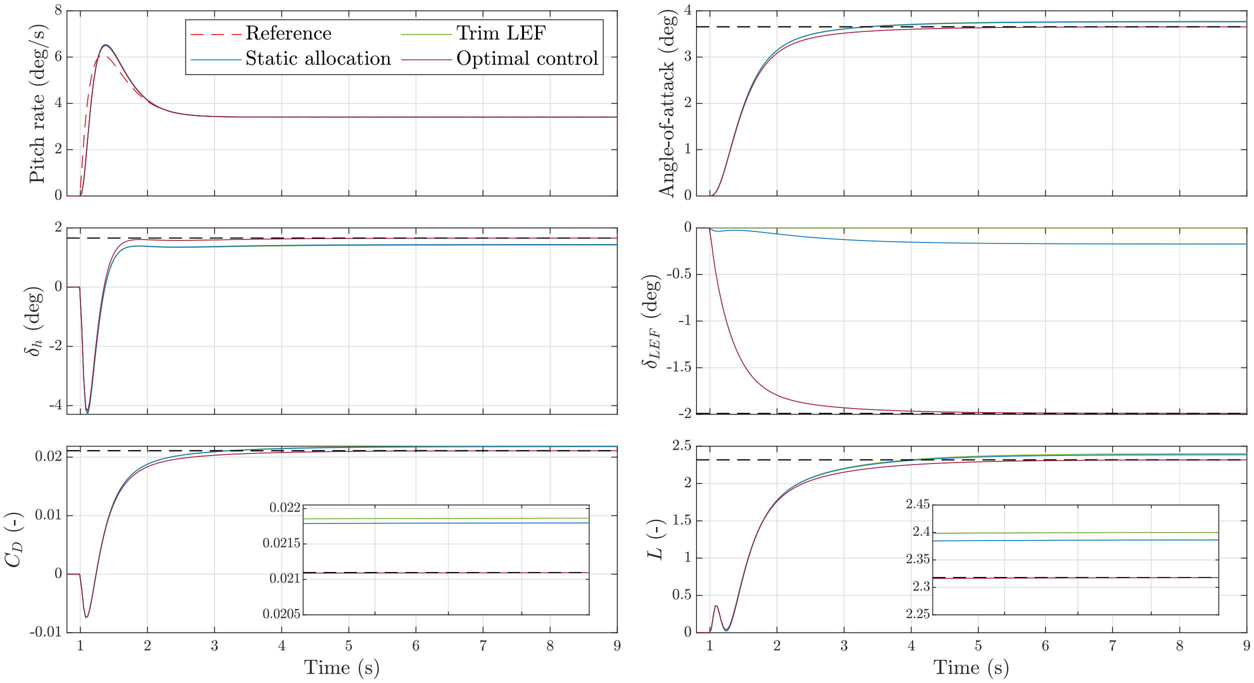

Fig. 2 Linear step response obtained for flight condition #1 (V_0 = 500 ft/s or M0.46, h = 10,000 ft); dashed lines indicate the true optimal steady-state solution

control law. This provides an additional perspective to the assessment of the multi-objective control laws. The true optimal control solution has been indicated in the figure as well. This solution can be straightforwardly obtained from

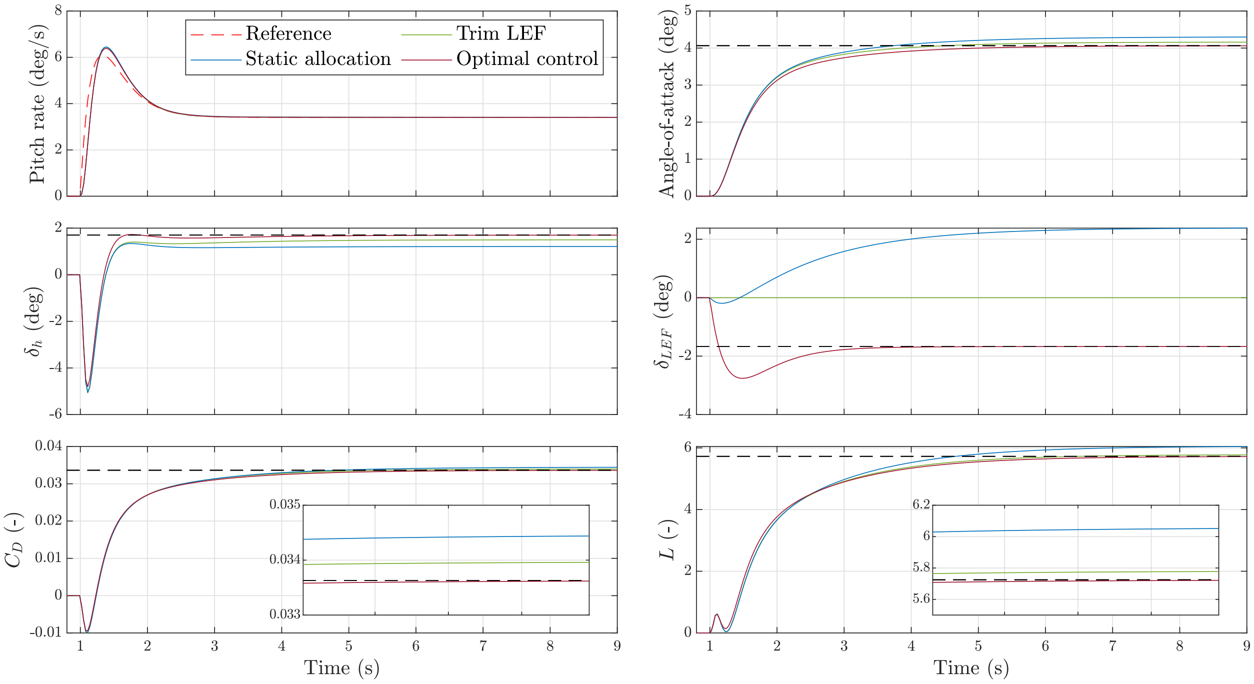

Fig. 3 Linear step response obtained for flight condition #2 (V_0 = 450 ft/s or M0.40, h = 10,000 ft); dashed lines indicate the true optimal steady-state solution

the system's equation of motion and the secondary objective function.

At first glance, it appears that the overall difference in response across the three control laws is limited. This is desirable in terms of the pitch response, which is effectively equivalent thanks to the kernel projection of the secondary control. The error with respect to the reference model can be largely attributed to the dynamics of the actuators, which have been neglected in the control design. Both multi-objective control laws command the leading edge flap to retract by a certain amount with respect to its initial position during the pull-up maneuver. When focusing on the steady-state response, this results in a slight reduction in the secondary performance index L which is paralleled by a small reduction in drag. Whereas the incremental optimal control law successfully drives the secondary objective to its optimal value, this is not achieved by the control allocation design. This is evident from the fact that long-term state-induced or setpoint-induced variations in the objective are not accounted for by the static control allocator.

This observation becomes more prominent in the second flight condition (V_0 = 450 ft/s or M0.40, h = 10,000 ft), for which the simulation results are displayed in Figure 3. The pitch rate tracking performance is again effectively equivalent, but the secondary performance index shows some important differences. In this case, it appears that the performance achieved by the benchmark is just slightly worse than the true optimum. This true optimum is again reached by the optimal control law. However, the static control allocator performs substantially worse compared to the benchmark case. This demonstrates that this design approach may not be suitable in case the secondary performance objective is strongly influenced by the dynamics of the system.

C. Robustness to synthesis model variations

The need for additional a-priori information of the plant dynamics is inherent to the multi-objective nature of the presented control laws. This is despite the assumption that direct ideal estimates of the secondary performance vector $\boldsymbol{\sigma}$ are available. This applies in particular to the kernel-constrained optimal control design, which requires a complete synthesis model of the IDI closed-loop dynamics in the construction of the performance feedback gains. The latter is in stark contrast to the philosophy of INDI-based design, which aims at reducing the dependency of the control system on detailed system models. Equations 46 and 48 provide some essential insights for this discussion. Although the secondary optimal control is derived after the primary control loop has been closed, the fact that the state feedback matrix T (and therefore the bare airframe state matrix A) appears directly in the augmented system formulation shows that the robustness benefits of reduced model dependency do not apply to the the secondary optimal control design presented here. This raises concerns regarding the control law's sensitivity to synthesis model variations.

A basic assessment of this sensitivity is performed based on the simulation results displayed in Figure 4. These results are obtained for different permutations where each control coefficient is varied by ±50% with respect to its nominal value. Several observations are highlighted here. Firstly, the results show that primary control task performance is retained under uncertainty in the A, C_σ, and D_σ matrices. Hence, the benefits of isolating primary and secondary control tasks are retained in these scenarios. Evidently, this does not hold in case the uncertainty appears in the effectiveness matrix B. This is due to the negative impact on the pseudo-inverse and kernel projection matrices. Secondly, despite the fact that direct measurements of $\boldsymbol{\sigma}$ are used, uncertainty in the C_σ-matrix leads to some variation in the response generated by the optimal control design. This is due to the fact that the C_σ-matrix appears in the Riccati equation. By contrast, although not included in Figure 4, the static allocation scheme remains invariant to system-dependent variations in this matrix. Thirdly, uncertainty in the synthesis A-matrix has a substantial impact on the secondary performance index of the optimal control law. This is again due to its central position in the Riccati equation. By comparison, the sensitivity to variations in the feedthrough matrix D_σ remain more benign.

D. Stability margins

In addition to assessing robustness in the time domain, it is of interest how the stability margins of the kernel-constrained controllers are affected compared to the benchmark IDI design. This is done by investigating the broken-loop response at several locations of the control law. The results are shown in Figure 5. The locations where each loop is broken have been annotated in the control system overview in Figure 1, where the numbering corresponds to the subfigure numbering used here. The loop shapes obtained for the pseudo-control vector (Figure 5a) and acceleration error (Figure 5b) give an indication of the stability margins at the level of the primary IDI control loop. Likewise, the response obtained at the effector level (Figures 5c and 5d) provides insight into the stability properties of the total control law.

Inspection of the broken-loop response diagrams shows there is very little variation of the response visible around crossover, which is a confirmation that robustness characteristics and short-term handling qualities associated with the

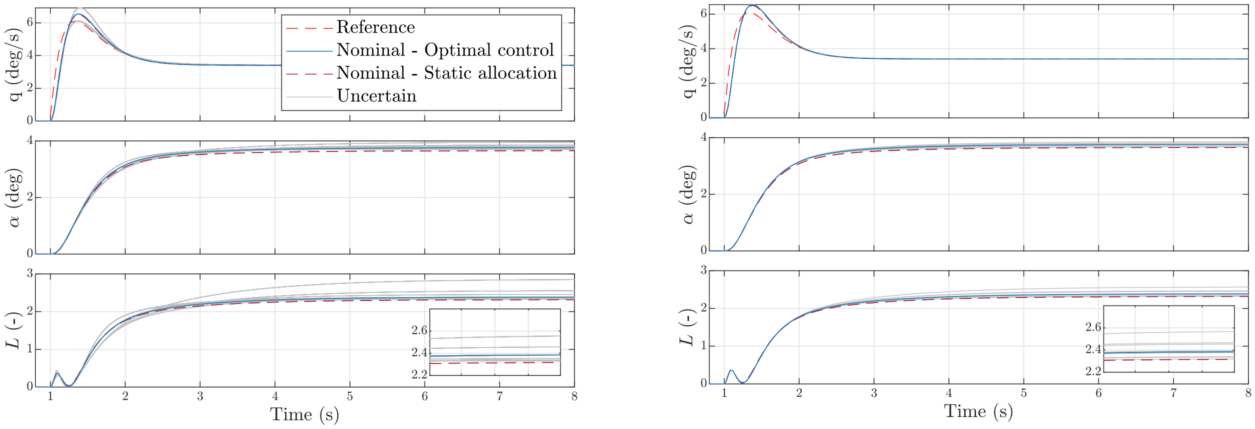

(a) Static control allocation; ΔB

(b) Static control allocation; $\Delta C_{D_{\delta_h}}$, $\Delta C_{D_{\delta_{LEF}}}$

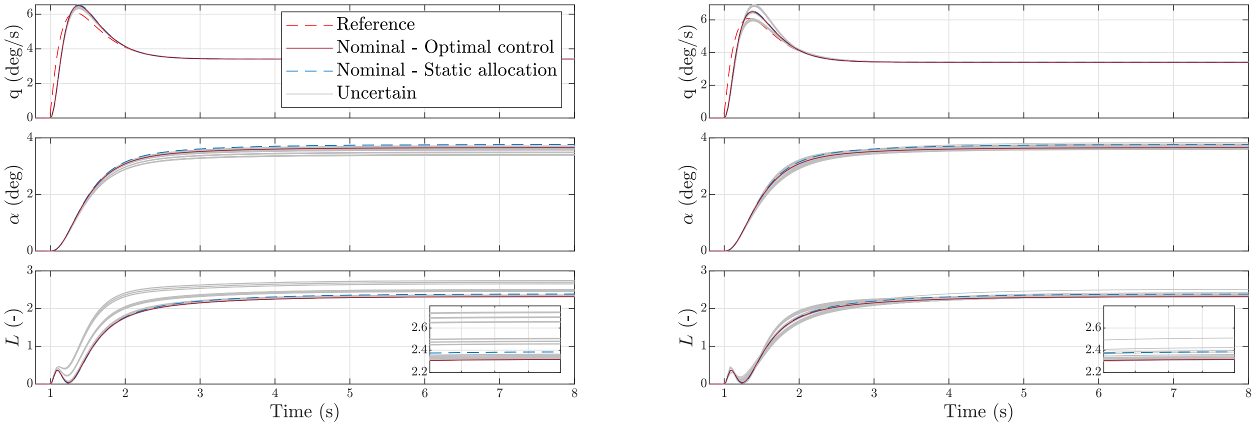

(c) Optimal control; ΔA

(d) Optimal control; ΔB

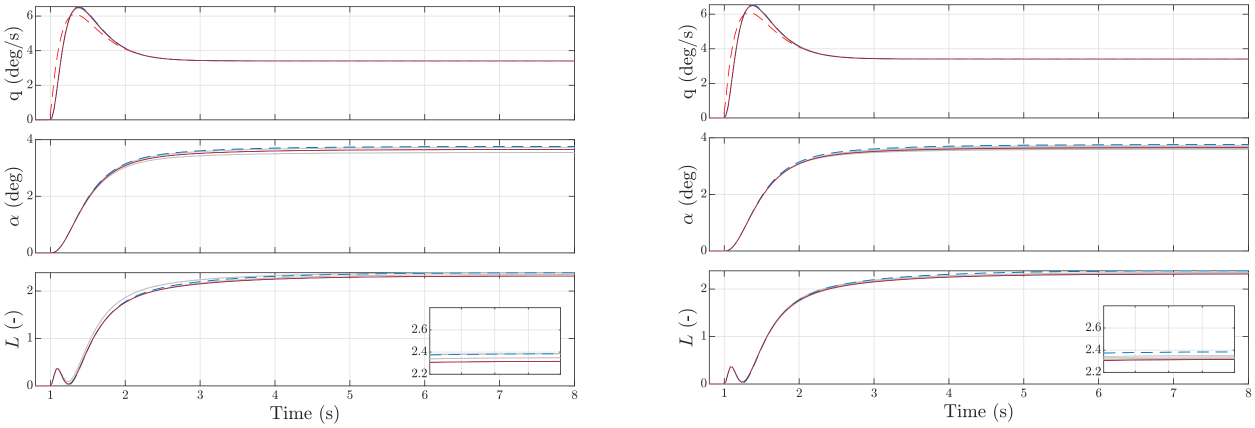

(e) Optimal control; ΔC_{D_α}, ΔC_{D_q}

(f) Optimal control; $\Delta C_{D_{\delta_h}}$, $\Delta C_{D_{\delta_{LEF}}}$

Fig. 4 Sensitivity to synthesis model coefficient variations of ±50% (flight cond. #1; V_0 = 500 ft/s, h = 10,000 ft)

control law are largely insensitive to the selected control strategy. Some variation is observed at low frequencies in the broken-loop responses associated with the horizontal tailplane and leading edge flap actuation paths. This observation is immediate from the fact that control effector gain is a direct function of control strategy. Moreover, it can be seen that both designs show a relatively low overall LEF loop gain. This implies that stability robustness properties are very adequate for this channel.

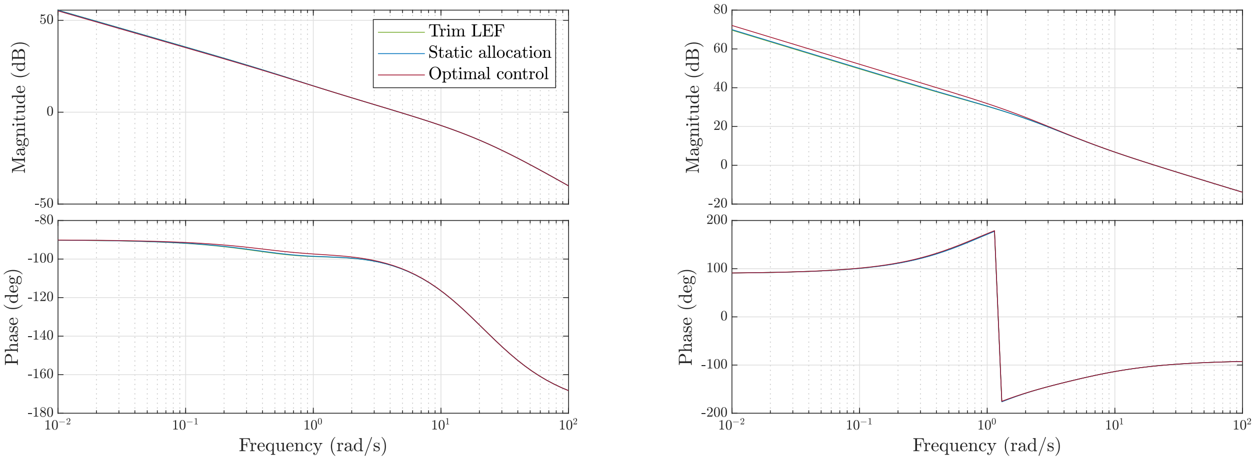

(a) Pseudo-control ν

(b) Acceleration error τ

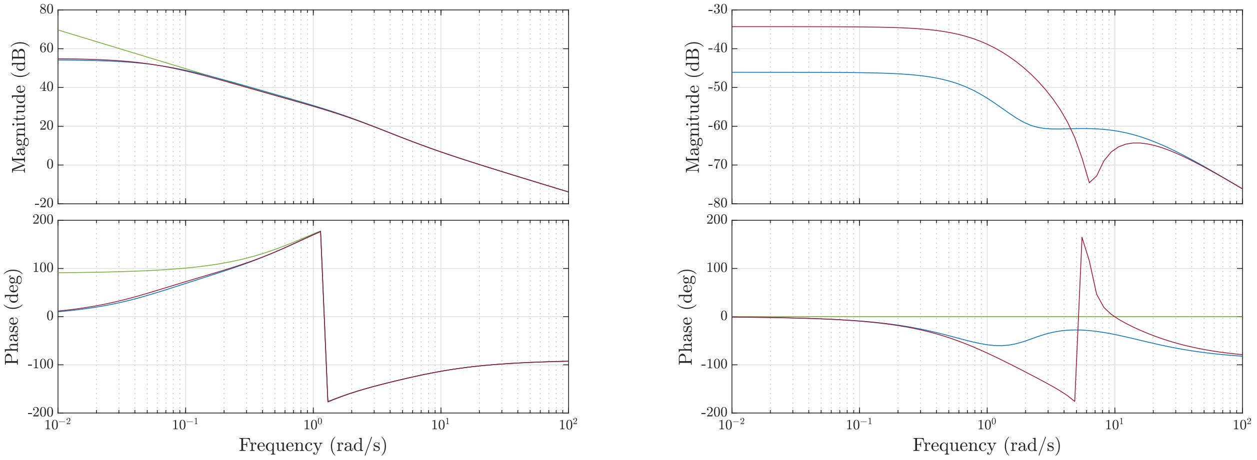

(c) Horizontal tail position δ_h

(d) LEF position δ_{LEF}

Fig. 5 Broken-loop responses (flight condition #1; V_0 = 500 ft/s or M0.46, h = 10,000 ft))

V. Nonlinear Control Allocation Simulation Results

In this section, nonlinear simulation results obtained using the kernel-projected incremental nonlinear control allocation (INCA) design will be discussed. In this case, the control law will exploit the nonlinear nature of the performance control effectiveness to optimize effector configurations such that the control-induced performance loss is minimized at every timestep. As demonstrated in the previous section, this strategy may generally not result in desirable control solutions in dynamic situations. Accordingly, a secondary nonlinear optimal control law is expected to results in better performance in these scenarios. Nevertheless, it remains of interest to analyze the behavior of the allocation scheme in a nonlinear context.

A. Control law extensions

Some extensions to the basic control law are discussed first. These include evaluation of the local control effectiveness, saturation handling, and estimation of the overall airframe drag.

1. Control effectiveness on-board model

The force and moment coefficients stored in the aerodynamic database are not affine in the horizontal tail position. Therefore, a central difference scheme is applied to obtain the local control effectiveness at every time step:

$$\hat{C}_{\bullet_{\delta_h}}(\alpha,\beta,\delta_h) = \frac{C_\bullet(\alpha,\beta,\delta_h+\epsilon) - C_\bullet(\alpha,\beta,\delta_h-\epsilon)}{2\epsilon} \tag{56}$$

No such solutions are needed for the leading edge flap, which is modeled by affine relations in the aerodynamic database.

2. Saturation handling

The control allocation scheme presented in Section II.B does not take into account effector limits. Neglecting these may have serious consequences on overall control law safety and performance, as the incremental demand equality constraint will not be met in case of saturation. Additional redistribution logic [11] is set in place to manage these situations. In case an input generated by the default control allocation logic exceeds one or more effector position limits, a scaling factor is calculated that scales the input vector such that it remains within the available input space:

$$k_s \Delta \boldsymbol{u}_k + \boldsymbol{u}_{k-1} \in \mathcal{U} \tag{57}$$

Subsequently, this scaling factor is adopted to generate the demand and gradient residuals:

$$\boldsymbol{\tau}'_k = (1-k_s)\boldsymbol{\tau}_k, \quad \boldsymbol{L}'_{\boldsymbol{u},k} = (1-k_s)\boldsymbol{L}_{\boldsymbol{u},k} \tag{58}$$

In addition, the P' and N' matrices are recalculated by setting the appropriate rows and columns of $\mathcal{B}$ and R equal to zero. Then, an additional control increment is computed as follows:

$$\Delta \boldsymbol{u}'_k = P'_k \boldsymbol{\tau}'_k - N'_k (R'_k)^{-1} \boldsymbol{L}'_{\boldsymbol{u},k} \tag{59}$$

Which leaves the total incremental control command as:

$$\Delta \boldsymbol{u}_k = k_s \Delta \boldsymbol{u}_k + \Delta \boldsymbol{u}'_k \triangleq \Delta \breve{\boldsymbol{u}}_k \tag{60}$$

If it turns out that $\boldsymbol{u}_k \notin \mathcal{U}$, the process will be repeated with a different k_s for $\Delta \breve{\boldsymbol{u}}_k$ until all effector limits are met. It should be noted that rate limits are not considered here; however, these could be incorporated relatively easily as suggested in [6, 12].

3. Drag coefficient estimation

In the nonlinear simulation scenario, the drag coefficient contribution to the performance vector will be estimated based on IMU and thrust measurements:

$$\hat{C}_X = \frac{mg}{\bar{q}S} n_x^{CG} - \frac{1}{\bar{q}S} T, \quad \hat{C}_Y = \frac{mg}{\bar{q}S} n_y^{CG}, \quad \hat{C}_Z = -\frac{mg}{\bar{q}S} n_z^{CG} \tag{61}$$

which are then transformed from the body-fixed to the aerodynamic reference frame using the kinematic relationships

$$\hat{C}_D = -\cos(\alpha)\cos(\beta)\hat{C}_X - \sin(\beta)\hat{C}_Y - \sin(\alpha)\cos(\beta)\hat{C}_Z \tag{62}$$

The rationale behind this estimation scheme is to reduce the level of model dependency in the control law. Nevertheless, adequate knowledge of aircraft mass and air data variables remains required for good estimation performance. In general, this information may not be straightforward to obtain in real-time. However, this will not be further considered in the analysis here. Therefore, the estimated drag coefficient equals the true drag coefficient returned by the simulation aerodynamic database in the presented nonlinear simulation scenarios.

B. Nominal scenario

The nominal performance of the control law is examined in a nonlinear simulation scenario with the starting condition corresponding to flight condition #1 (V_0 = 500 ft/s or M0.46, h = 10,000 ft). The engine throttle is set all the way back to idle at the start of the simulation, whereas a push-up/pull-over (PUPO) maneuver is executed by the pilot after several seconds. This scenario allows a separate investigation of both the primary and secondary control features, since the aircraft will experience changing flight conditions in the absence of pilot stick input.

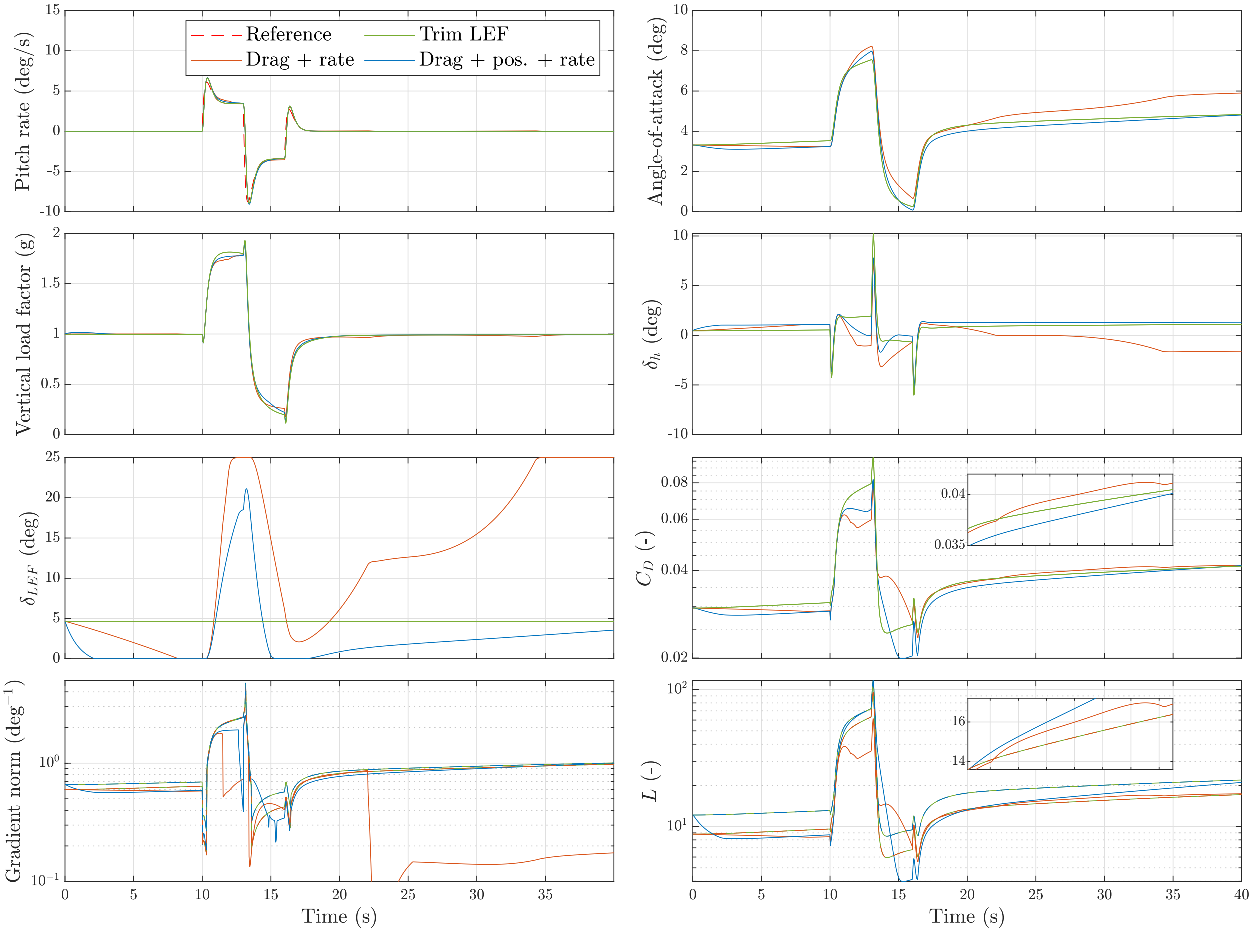

Fig. 6 Nominal nonlinear simulation time histories obtained for the kernel-based restoring INCA and benchmark INDI control law designs

Three control law designs are evaluated. These include the INDI benchmark controller that leaves the LEF in trim configuration and two INCA-based variants. One variant only considers drag and control increment weighting in the objective function ($C_{D_{ref}} = 0.01$, $W_p^{1/2} = diag(0, 0)$, and $W_r = 0.25diag(0.1, 1)$), whereas the other variant is equivalent to the design evaluated in Section IV and therefore also penalizes effector position to reduce control activity ($C_{D_{ref}} = 0.01$, $W_p^{1/2} = 5diag(\frac{1}{\bar{\delta}_h - \underline{\delta}_h}, \frac{1}{\bar{\delta}_{LEF} - \underline{\delta}_{LEF}})$, and $W_r = 0.25diag(0.1, 1)$). Figure 6 shows the simulation time histories for each control design.

A first observation is that the aircraft's pitch rate adequately tracks the reference trajectory for all control laws. Therefore, the primary control objective is achieved with any of these designs. Regarding the secondary performance index, a more intricate discussion is at hand. Therefore, the simulation outcomes will be examined in three parts: the pre-maneuver phase ($0 \le t < 10$ s), the maneuver phase ($10 \le t < 20$ s), and the post-maneuver phase ($20 \le t \le 40$ s).

In the pre-maneuver phase, both INCA designs lead to improved performance over the benchmark INDI control law. Both designs retract the LEF with respect to its initial trim position, which results in a reduction of the input gradient norm $\|\boldsymbol{L_u}\|_2$ as well as the performance index L. The angle-of-attack steadily increases due the decreasing airspeed as a result of idle thrust. However, this increase is partially offset by the INCA designs as a by-product of retracing the LEF. Consequently, the pilot initiates the pull-up part of the maneuver. The INCA control laws command large LEF deflections to minimize the input gradient norm, which again results in a subsequent reduction in the performance index and drag coefficient when compared to the benchmark. When looking in more detail at the push-over part, it is observed that more or less the same trend applies to the position-weighted INCA design whereas the control law which disregards effector position performs mostly worse than the benchmark. The latter can be largely explained by the fact that the control law pushes the aircraft to higher angle-of-attack levels.

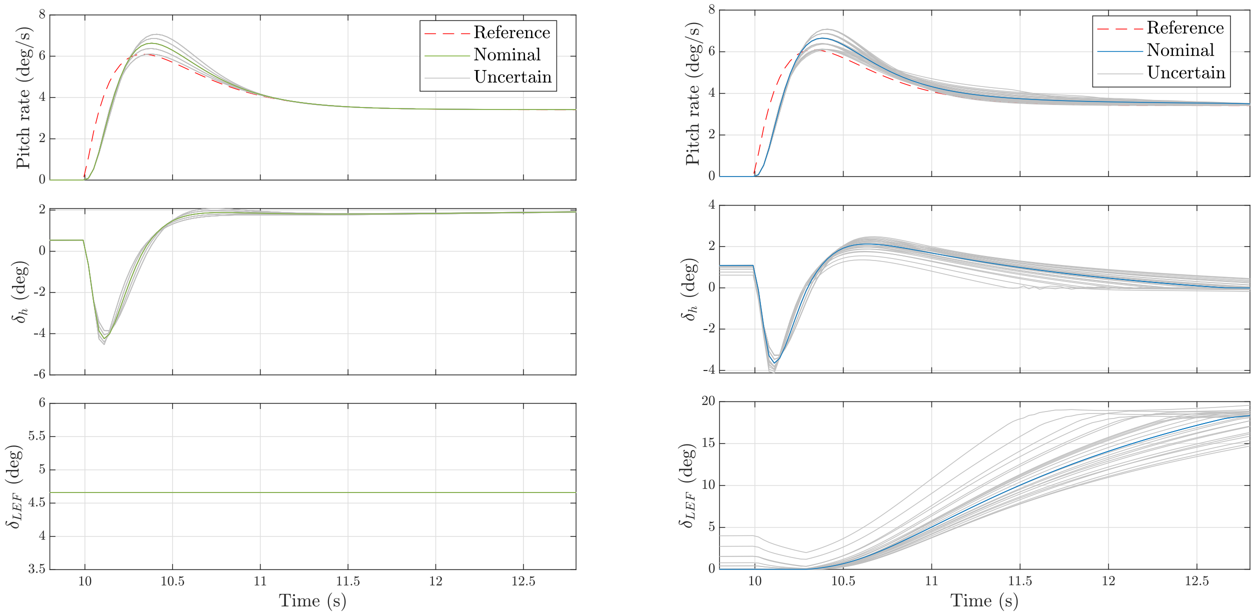

(a) Benchmark INDI design

(b) INCA with kernel restoring (drag + pos. + rate)

Fig. 7 Nonlinear simulation time histories obtained for control effectiveness on-board model offsets up to ±50%

This last observation also applies to the third and final phase of the simulation, the post-maneuver part. In an effort to further reduce the input gradient norm, the position-unweighted design further extends the leading edge flap until its maximum position is reached. This again causes the angle-of-attack to increase. Evidently, this effect is not respected by static allocation. It is observed that the extra drag caused by angle-of-attack destroys the gain of lower control-induced drag. The result is a larger overall drag coefficient compared to the benchmark design. These effects are not immediately visible for the position-weighted design. Based on the insights from the previous linear analysis, an improvement in secondary control performance would be expected if the control law would have been designed according to the principles of the kernel-projected incremental optimal control concept.

C. Sensitivity to control effectiveness mismatch

In this section, the focus is on nonlinear primary control performance in case the on-board model representations of the control effectiveness terms $\hat{C}_{m_{\delta_h}}$ and $\hat{C}_{m_{\delta_{LEF}}}$ are not equal to their true values. It is concluded from the simulation results from Figure 6 that the nonlinear nature of the control problem causes the effector activity to increase substantially with respect to the linear designs in Section IV. Therefore, it is of interest to examine how this increased activity affects the primary control task in the presence of uncertainty. Figure 7 displays the pitch rate and control effector position variations obtained using the benchmark INDI and position-weighted INCA designs. It is evident that incorporation of the secondary control task in the controller design results in additional variation of the pitch rate response under uncertainty. This is again a direct result of the effect on the pseudo-inverse and kernel projection matrices.

VI. Conclusion

Several achievements in this work can be listed. Firstly, an extension to the existing Incremental Nonlinear Control Allocation (INCA) framework was presented for over-determined control problems. This formulation adds a kernel-based effector restoring functionality in the context of arbitrary secondary objectives without affecting primary control law performance. In other words, this concept does not require combined objective function formulations that lead to unwanted trade-offs between primary and secondary control tasks. Secondly, an alternative, but closely related framework based on kernel-projected optimal control was formulated that extends the traditional scope of control allocation to situations where secondary control task requires active control of the bare airframe system dynamics. Several multi-objective control laws based on these methods were designed for a secondary performance objective consisting of a weighted least-squares combination of the overall airframe drag coefficient and effector activity. It was shown that the INCA-based design does not always result in desirable control solutions as a result of the strong impact of angle-of-attack on the secondary control task. This is evident from the fact that state-induced variations are not accounted for in a dynamic sense by the static allocator. The concept of kernel-projected incremental optimal control provides the necessary instruments to deal with these scenarios.

Several recommendations for further research are in place here. Firstly, the kernel-projected optimal control concept was applied in a linear context only. The nonlinear form that was presented does not include a description of the costate variable. Therefore, a natural follow-up research activity is to further develop this design method such that it can be used in nonlinear flight control problems as well. A second relevant direction for further investigation is to design for improved robustness levels. Thirdly, the interaction between the primary and secondary control law loops should be investigated in more detail. Although the kernel projection ensures that these are decoupled through the control effectiveness matrix, there are other interaction mechanisms that must be considered. For example, the secondary control law has a direct impact on the zero dynamics associated with the dynamic inversion control system. Oppositely, the selected dynamic inversion design has an impact on the design of the secondary controller as well.

Appendix

The system described by Equations 39, 42, and 46-48 leads to the following formulation of the Hamiltonian:

$$\begin{aligned}\mathcal{H}(z_k, \Delta\boldsymbol{u}_k^{\perp}, \boldsymbol{r}_k, \tilde{\boldsymbol{\lambda}}_{k+1}) = \frac{1}{2}\left\|Y_\sigma z_k + D_\sigma P\boldsymbol{r}_k + D_\sigma \Delta\boldsymbol{u}_k^{\perp}\right\|_2^2 + \frac{1}{2}\left\|W_r^{1/2}\left(P\boldsymbol{r} - PT_* z_k + \Delta\boldsymbol{u}_k^{\perp}\right)\right\|_2^2 + \\ \tilde{\boldsymbol{\lambda}}_{k+1}^T\left(A_{c_*} z_k + B_*\Delta\boldsymbol{u}_k^{\perp} + B_* P\boldsymbol{r}_k\right)\end{aligned} \tag{63}$$

where $T_* \triangleq \begin{bmatrix} T & C_y B\end{bmatrix}$. Note that the above Hamiltonian function reflects the fact that the optimal control for the *secondary* control increment must be found. Moreover, it is emphasized that the derivation effectively continues the steps outlined in Section II.C. In this regard, optimality with respect to both the static Langrange multiplier and the stationarity condition has been achieved through the selected form of the control law. Therefore, the remaining necessary conditions for optimality are the following [23]:

$$z_{k+1} = \frac{\partial\mathcal{H}(z_k, \Delta\boldsymbol{u}_k^{\perp}, \boldsymbol{r}_k, \tilde{\boldsymbol{\lambda}}_{k+1})}{\partial\tilde{\boldsymbol{\lambda}}_{k+1}} \tag{64}$$

$$\tilde{\boldsymbol{\lambda}}_k = \frac{\partial\mathcal{H}(z_k, \Delta\boldsymbol{u}_k^{\perp}, \boldsymbol{r}_k, \tilde{\boldsymbol{\lambda}}_{k+1})}{\partial z_k} \tag{65}$$

The first condition represents the state equation described by Equation 46. Substituting the orthogonal control increment expressed in Equation 47 results in the following formulation:

$$z_{k+1} = \left(A_{c_*} + E\right) z_k - F\tilde{\boldsymbol{\lambda}}_{k+1} + B_* P\boldsymbol{r}_k \tag{66}$$

where

$$E \triangleq -B_* N R^{-1} D_\sigma^T V_\sigma \quad , \quad F \triangleq B_* N R^{-1} B_*^T \tag{67}$$

The second condition leads to the costate equation or adjoint system description and is expressed as follows:

$$\tilde{\boldsymbol{\lambda}}_k = Y_\sigma^T\left(Y_\sigma z_k + D_\sigma P\boldsymbol{r}_k + D_\sigma\Delta\boldsymbol{u}_k^{\perp}\right) + \left(PT_*\right)^T W_r\left(PT_* z_k - P\boldsymbol{r}_k - \Delta\boldsymbol{u}_k^{\perp}\right) + A_{c_*}^T\tilde{\boldsymbol{\lambda}}_{k+1} \tag{68}$$

Again substituting the orthogonal control increment from Equation 47 leads to the recursive equation

$$\tilde{\boldsymbol{\lambda}}_k = H z_k + \left(A_{c_*}^T + G\right)\tilde{\boldsymbol{\lambda}}_{k+1} + \left(Y_\sigma^T D_\sigma - P^T T_*^T W_r\right) P\boldsymbol{r}_k \tag{69}$$

where G and H are defined as in Equation 51. Consequently, Equations 66 and 69 represent a nonhomogenous Hamiltonian system description [23]:

$$\begin{bmatrix} I & F \\ 0 & A_{c_*}^T + G\end{bmatrix}\begin{bmatrix} z_{k+1} \\ \tilde{\boldsymbol{\lambda}}_{k+1}\end{bmatrix} = \begin{bmatrix} A_{c_*} + E & 0 \\ -H & I\end{bmatrix}\begin{bmatrix} z_k \\ \tilde{\boldsymbol{\lambda}}_k\end{bmatrix} + \begin{bmatrix} B_* \\ P^T T_*^T W_r - Y_\sigma^T D_\sigma\end{bmatrix} P\boldsymbol{r}_k \tag{70}$$

The state and costate sequences that satisfy this system must now be established. It will be assumed [23] that the costate is of the form $\tilde{\boldsymbol{\lambda}}_k = S_k z_k + \boldsymbol{v}_k$, which leads to the following formulation of the costate equation:

$$S_k \boldsymbol{z}_k + \boldsymbol{v}_k = H \boldsymbol{z}_k + \left(A_{c_*}^T + G\right)\left(S_{k+1} \boldsymbol{z}_{k+1} + \boldsymbol{v}_{k+1}\right) + \left(Y_\sigma^T D_\sigma - P^T T_*^T W_r\right) P \boldsymbol{r}_k \tag{71}$$

Substituting Equation 46 yields:

$$S_k \boldsymbol{z}_k + \boldsymbol{v}_k = H \boldsymbol{z}_k + \left(A_{c_*}^T + G\right)\left(S_{k+1} A_{c_*} \boldsymbol{z}_k + S_{k+1} B_* \Delta \boldsymbol{u}_k^\perp + S_{k+1} B_* P \boldsymbol{r}_k + \boldsymbol{v}_{k+1}\right) + \left(Y_\sigma^T D_\sigma - P^T T_*^T W_r\right) P \boldsymbol{r}_k \tag{72}$$

Likewise, the orthogonal incremental optimal control corresponding to the selected costate description is written as:

$$\Delta \boldsymbol{u}_k^\perp = -\tilde{R}_{k+1}^{-1} N R^{-1} \left[\left(D_\sigma^T V_\sigma + B_*^T S_{k+1} A_{c_*}\right) \boldsymbol{z}_k + B_*^T S_{k+1} B_* P \boldsymbol{r}_k + B_*^T \boldsymbol{v}_{k+1}\right] \tag{73}$$

where $\tilde{R}_{k+1} \triangleq I + N R^{-1} B_*^T S_{k+1} B_*$. Substituting Equation 73 into Equation 72 results in

$$\begin{aligned} S_k \boldsymbol{z}_k + \boldsymbol{v}_k = H \boldsymbol{z}_k + \left(Y_\sigma^T D_\sigma - P^T T_*^T W_r\right) P \boldsymbol{r}_k + \left(A_{c_*}^T + G\right) \big(& S_{k+1} A_{c_*} \boldsymbol{z}_k + S_{k+1} B_* P \boldsymbol{r}_k + \boldsymbol{v}_{k+1} - \\ & S_{k+1} B_* \tilde{R}_{k+1}^{-1} N R^{-1} \left[\left(D_\sigma^T V_\sigma + B_*^T S_{k+1} A_{c_*}\right) \boldsymbol{z}_k + B_*^T S_{k+1} B_* P \boldsymbol{r}_k + B_*^T \boldsymbol{v}_{k+1}\right]\big) \end{aligned} \tag{74}$$

Collecting terms:

$$\begin{aligned} & \left[-S_k + H + \left(A_{c_*}^T + G\right) S_{k+1} \left(A_{c_*} - B_* \tilde{R}_{k+1}^{-1} N R^{-1} \left(D_\sigma^T V_\sigma + B_*^T S_{k+1} A_{c_*}\right)\right)\right] \boldsymbol{z}_k + \\ & \left(Y_\sigma^T D_\sigma - P^T T_*^T W_r + \left(A_{c_*}^T + G\right) S_{k+1} B_* \left(I - \tilde{R}_{k+1}^{-1} N R^{-1} B_*^T S_{k+1} B_*\right)\right) P \boldsymbol{r}_k + \\ & \left(A_{c_*}^T + G\right) \left(I - S_{k+1} B_* \tilde{R}_{k+1}^{-1} N R^{-1} B_*^T\right) \boldsymbol{v}_{k+1} - \boldsymbol{v}_k = 0 \end{aligned} \tag{75}$$

This expression must hold for all states $\boldsymbol{z}_k$ and reference signals $\boldsymbol{r}_k$. Therefore [23], the following expressions apply:

$$S_k = H + \left(A_{c_*}^T + G\right) S_{k+1} \left(A_{c_*} - B_* \tilde{R}_{k+1}^{-1} N R^{-1} \left(D_\sigma^T V_\sigma + B_*^T S_{k+1} A_{c_*}\right)\right) \tag{76}$$

and

$$\begin{aligned} \boldsymbol{v}_k = \left(Y_\sigma^T D_\sigma - P^T T_*^T W_r + \left(A_{c_*}^T + G\right) S_{k+1} B_* \left(I - \tilde{R}_{k+1}^{-1} N R^{-1} B_*^T S_{k+1} B_*\right)\right) P \boldsymbol{r}_k + \\ \left(A_{c_*}^T + G\right) \left(I - S_{k+1} B_* \tilde{R}_{k+1}^{-1} N R^{-1} B_*^T\right) \boldsymbol{v}_{k+1} \end{aligned} \tag{77}$$

In order to find the optimal control sequence, the above difference equations shall be solved for the appropriate boundary conditions. The goal here is to arrive at the infinite time-horizon optimal control law. Therefore, use will be made of the steady-state (invariant) solutions $S_k = S_{k+1} = S$ and $\boldsymbol{v}_k = \boldsymbol{v}_{k+1} = \boldsymbol{v}$. This results in the algebraic Riccati equation

$$-S + H + \left(A_{c_*}^T + G\right) S \left(A_{c_*} - B_* \tilde{R}^{-1} N R^{-1} \left(D_\sigma^T V_\sigma + B_*^T S A_{c_*}\right)\right) = 0 \tag{78}$$

which is equivalent to Equation 50; moreover,

$$\begin{aligned} -\boldsymbol{v} + \left(Y_\sigma^T D_\sigma - P^T T_*^T W_r + \left(A_{c_*}^T + G\right) S B_* \left(I - \tilde{R}^{-1} N R^{-1} B_*^T S B_*\right)\right) P \boldsymbol{r}_k + \\ \left(A_{c_*}^T + G\right) \left(I - S B_* \tilde{R}^{-1} N R^{-1} B_*^T\right) \boldsymbol{v} = \boldsymbol{0} \end{aligned} \tag{79}$$

where $\tilde{R} \triangleq I + N R^{-1} B_*^T S B_*$. Equation 79 can be used immediately to derive an analytical expression for $\boldsymbol{v}$:

$$\boldsymbol{v} = V^{-1} U P \boldsymbol{r}_k \tag{80}$$

with U and V defined as in Equation 53. Now, the matrix S that solves Equation 78 will be obtained using the Schur vector approach [29, 30]. To this end, the homogenous part of the Hamiltonian system described by Equation 70 is used:

$$\underbrace{\begin{bmatrix} I & F \\ 0 & A_{c_*}^T + G \end{bmatrix}}_{\triangleq L} \begin{bmatrix} \boldsymbol{z}_{k+1} \\ \tilde{\boldsymbol{\lambda}}'_{k+1} \end{bmatrix} = \underbrace{\begin{bmatrix} A_{c_*} + E & 0 \\ -H & I \end{bmatrix}}_{\triangleq M} \begin{bmatrix} \boldsymbol{z}_k \\ \tilde{\boldsymbol{\lambda}}'_k \end{bmatrix} \tag{81}$$

where $\tilde{\lambda}'_k \triangleq S\boldsymbol{z_k}$. The solution of this system of difference equations can be obtained by solving the generalized eigenvalue problem

$$M\mathbf{v} = sL\mathbf{v} \tag{82}$$

The Schur vector approach requires the real Schur form of M and L, which can be obtained through QZ factorization of the above generalized eigenvalue problem. This results in the following matrix pencil [30]:

$$Q\left(M - sL\right)Z = \tilde{M} - s\tilde{L} \tag{83}$$

where $\tilde{M}$ and $\tilde{L}$ are quasi-triangular and Q and Z are unitary matrices. Denoting $n_z = \dim(\boldsymbol{z}_k)$, this decomposition shall be arranged such that the generalized eigenvalues corresponding to the interior of the unit disk appear in the upper left $n_z \times n_z$ blocks of the quasitriangular pair ($\tilde{M}$,$\tilde{L}$). Recognizing that Z takes the form of four $n_z \times n_z$ blocks [29, 30]:

$$Z = \begin{bmatrix} Z_{11} & Z_{12} \\ Z_{21} & Z_{22} \end{bmatrix} \tag{84}$$

Then, the Schur vectors $\begin{bmatrix} Z_{11} & Z_{21} \end{bmatrix}^T$ span the basis of the stable subspace associated with the Hamiltonian system. Consequently, the stabilizing matrix S that solves Equation 78 is given by [29, 30]:

$$S = Z_{21}Z_{11}^{-1} \tag{85}$$

With this last step, all information that is required to construct the infinite time-horizon orthogonal optimal control has been obtained. From Equations 73 and 80, this leads to the final result

$$\Delta\boldsymbol{u}_k^{\perp} = -\tilde{R}^{-1}NR^{-1}\left[\left(D_{\sigma}^T V_{\sigma} + B_*^T S A_{c_*}\right)\boldsymbol{z}_k + B_*^T\left(SB_* + V^{-1}U\right)P\boldsymbol{r}_k\right] \tag{86}$$

which produces the total control law described by Equation 52.

References

[1] Delannoy, S., "A380 Roll Kinematics Design," *IFAC Proceedings Volumes*, Vol. 40, No. 7, 2007, pp. 103–108. https://doi.org/10.3182/20070625-5-FR-2916.00019, 17th IFAC Symposium on Automatic Control in Aerospace.

[2] Scalera, K., and Durham, W., "A comparison of control allocation methods for the F-15 ACTIVE research aircraft utilizing real-time piloted simulations," *Guidance, Navigation, and Control Conference and Exhibit*, Portland, OR, USA, 1999. https://doi.org/10.2514/6.1999-4281, AIAA-1999-4281.

[3] Steinhauser, R., Looye, G., and Brieger, O., "Design and Evaluation of Control Laws for the X-31A with Reduced Vertical Tail," *AIAA Guidance, Navigation, and Control Conference and Exhibit*, Providence, RI, USA, 2004. https://doi.org/10.2514/6.2004-5031, AIAA-2004-5031.

[4] Bordignon, K., and Bessolo, J., "Control Allocation for the X-35B," *2002 Biennial International Powered Lift Conference and Exhibit*, Williamsburg, VA, USA, 2002. https://doi.org/10.2514/6.2002-6020, AIAA 2002-6020.

[5] Zhang, J., Bhardwaj, P., Raab, S. A., Saboo, S., and Holzapfel, F., "Control Allocation Framework for a Tilt-rotor Vertical Take-off and Landing Transition Aircraft Configuration," *2018 Applied Aerodynamics Conference*, Atlanta, GA, USA, 2018. https://doi.org/10.2514/6.2018-3480, AIAA 2018-3480.

[6] Durham, W., Bordignon, K., and Beck, R., *Aircraft Control Allocation*, John Wiley & Sons, 2016. https://doi.org/10.1002/9781118827789.

[7] Reckzeh, D., "Multifunctional Wing Moveables: Design of the A350XWB and the Way to Future Concepts," *Proceedings of the 29th Congress of the International Council of the Aeronautical Sciences (ICAS)*, St. Petersburg, Russia, 2014.

[8] Wagner, M., and Norris, G., *Boeing 787 Dreamliner*, Zenith Press, 2009.

[9] Durham, W., "Constrained control allocation," *Journal of Guidance, Control, and Dynamics*, Vol. 16, No. 4, 1993, pp. 717–725. https://doi.org/10.2514/3.21072.

[10] Oppenheimer, M. W., Doman, D. B., and Bolender, M. A., "Control Allocation for Over-actuated Systems," *2006 14th Mediterranean Conference on Control and Automation*, Ancona, Italy, 2006. https://doi.org/10.1109/MED.2006.328750.

[11] Johansen, T. A., and Fossen, T. I., “Control allocation — A survey,” *Automatica*, Vol. 49, No. 5, 2013, pp. 1087–1103. https://doi.org/10.1016/j.automatica.2013.01.035.

[12] Matamoros, I., and de Visser, C. C., “Incremental Nonlinear Control Allocation for a Tailless Aircraft with Innovative Control Effectors,” *2018 AIAA Guidance, Navigation, and Control Conference*, Kissimmee, FL, USA, 2018. https://doi.org/10.2514/6.2018-1116, AIAA 2018-1116.

[13] Miller, C. J., and Goodrick, D., “Optimal Control Allocation with Load Sensor Feedback for Active Load Suppression, Experiment Development,” *AIAA Guidance, Navigation, and Control Conference*, Grapevine, TX, USA, 2017. https://doi.org/10.2514/6.2017-1719, AIAA-2017-1719.

[14] Durham, W. C., Bolling, J. G., and Bordignon, K. A., “Minimum Drag Control Allocation,” *Journal of Guidance, Control, and Dynamics*, Vol. 20, No. 1, 1997, pp. 190–193. https://doi.org/10.2514/2.4018.

[15] Stolk, R., and de Visser, C. C., “Minimum drag control allocation for the Innovative Control Effector aircraft,” *Proceedings of the 2019 CEAS Specialist Conference on Guidance, Navigation and Control (EuroGNC)*, Milan, Italy, 2019.

[16] Pollack, T. S. C., and van Kampen, E., “Optimal Variable Wing Camber Control using Incremental Nonlinear Dynamic Inversion,” *Proceedings of the 2022 CEAS Specialist Conference on Guidance, Navigation and Control (EuroGNC)*, Berlin, Germany, 2022.

[17] Wang, X., van Kampen, E., Chu, Q., and Lu, P., “Stability Analysis for Incremental Nonlinear Dynamic Inversion Control,” *Journal of Guidance, Control, and Dynamics*, Vol. 42, No. 5, 2019, pp. 1116–1129. https://doi.org/10.2514/1.G003791.

[18] Bacon, B., and Ostroff, A., “Reconfigurable flight control using nonlinear dynamic inversion with a special accelerometer implementation,” *AIAA Guidance, Navigation, and Control Conference and Exhibit*, Denver, CO, USA, 2000. https://doi.org/10.2514/6.2000-4565, AIAA-2000-4565.

[19] Sieberling, S., Chu, Q. P., and Mulder, J. A., “Robust Flight Control Using Incremental Nonlinear Dynamic Inversion and Angular Acceleration Prediction,” *Journal of Guidance, Control, and Dynamics*, Vol. 33, No. 6, 2010, pp. 1732–1742. https://doi.org/10.2514/1.49978.

[20] Grondman, F., Looye, G., Kuchar, R., Chu, Q. P., and van Kampen, E., “Design and Flight Testing of Incremental Nonlinear Dynamic Inversion-based Control Laws for a Passenger Aircraft,” *2018 AIAA Guidance, Navigation, and Control Conference*, Kissimmee, FL, USA, 2018. https://doi.org/10.2514/6.2018-0385, AIAA 2018-0385.

[21] Nocedal, J., and Wright, S. J., *Numerical Optimization*, 2nd ed., Springer New York, NY, 2006. https://doi.org/10.1007/978-0-387-40065-5.

[22] Härkegård, O., and Glad, S. T., “Resolving actuator redundancy—optimal control vs. control allocation,” *Automatica*, Vol. 41, No. 1, 2005, pp. 137–144. https://doi.org/10.1016/j.automatica.2004.09.007.

[23] Lewis, F., Vrabie, D., and Syrmos, V., *Optimal Control*, 3rd ed., John Wiley & Sons, 2012. https://doi.org/10.1002/9781118122631.

[24] Härkegård, O., “Dynamic Control Allocation Using Constrained Quadratic Programming,” *Journal of Guidance, Control, and Dynamics*, Vol. 27, No. 6, 2004, pp. 1028–1034. https://doi.org/10.2514/1.11607.

[25] Nguyen, L. T., Ogburn, M. E., Gilbert, W. P., Kibler, K. S., Brown, P. W., and Deal, P. L., “Simulator Study of Stall/Post-Stall Characteristics of a Fighter Airplane With Relaxed Longitudinal Static Stability,” Tech. rep., National Aeronautics and Space Administration, Langley Research Center, Hampton, VA, USA, December 1979.

[26] Russel, R., “Non-linear F-16 Simulation using Simulink and Matlab,” Tech. rep., University of Minnesota, June 2003.

[27] Droste, C., and Walker, J., *The General Dynamics Case Study on the F-16 Fly-By-Wire Flight Control System*, American Institute of Aeronautics and Astronautics, 2010. https://doi.org/10.2514/4.867873.

[28] Anonymous, “Flying Qualities of Piloted Aircraft,” Tech. Rep. MIL-HDBK-1797A, U.S. Department of Defense (DoD), December 1997.

[29] Laub, A., “A Schur method for solving algebraic Riccati equations,” *IEEE Transactions on Automatic Control*, Vol. 24, No. 6, 1979, pp. 913–921. https://doi.org/10.1109/TAC.1979.1102178.

[30] Laub, A. J., “Schur techniques in invariant imbedding methods for solving two-point boundary value problems,” *1982 21st IEEE Conference on Decision and Control*, 1982, pp. 56–61. https://doi.org/10.1109/CDC.1982.268400.